Deep-Sea Research I 95 (2015) 20–36

Contents lists available at ScienceDirect

Deep-Sea Research I

journal homepage: www.elsevier.com/locate/dsri

Instruments and Methods

Development of a deep-sea laser-induced breakdown spectrometer for in situ multi-element chemical analysis

Blair Thornton [a,*], Tomoko Takahashi [a], Takumi Sato [a], Tetsuo Sakka [b], Ayaka Tamura [b], Ayumu Matsumoto [b], Tatsuo Nozaki [c], Toshihiko Ohki [a,d], Koichi Ohki [d]

[a] Institute of Industrial Science, The University of Tokyo, 4-6-1 Komaba, Meguro-ku, Tokyo 153-8505, Japan
[b] Department of Energy and Hydrocarbon Chemistry, Graduate School of Engineering, Kyoto University, Nishikyo-ku, Kyoto 615-8510, Japan
[c] Research and Development Center for Submarine Resources, Japan Agency for Marine-Earth Science and Technology, Yokosuka, Kanagawa 237-0061, Japan
[d] OK Lab. Co. Ltd., 8-7-3 Shimorenjyaku, Mitaka, Tokyo 181-0013, Japan

ARTICLE INFO

Article history:
Received 25 August 2014
Received in revised form
15 October 2014
Accepted 18 October 2014
Available online 29 October 2014

Keywords:
Laser-induced breakdown spectroscopy
In situ chemical analysis
Geochemistry
Remotely operated vehicle
Deep-sea

ABSTRACT

Spectroscopy is emerging as a technique that can expand the envelope of modern oceanographic sensors. The selectivity of spectroscopic techniques enables a single instrument to measure multiple components of the marine environment and can form the basis for versatile tools to perform in situ geochemical analysis. We have developed a deep-sea laser-induced breakdown spectrometer (ChemiCam) and successfully deployed the instrument from a remotely operated vehicle (ROV) to perform in situ multi-element analysis of both seawater and mineral deposits at depths of over 1000 m. The instrument consists of a long-nanosecond duration pulse-laser, a spectrometer and a high-speed camera. Power supply, instrument control and signal telemetry are provided through a ROV tether. The instrument has two modes of operation. In the first mode, the laser is focused directly into seawater and spectroscopic measurements of seawater composition are performed. In the second mode, a fiber-optic cable assembly is used to make spectroscopic measurements of mineral deposits. In this mode the laser is fired through a 4 m long fiber-optic cable and is focused onto the target's surface using an optical head and a linear stage that can be held by a ROV manipulator. In this paper, we describe the instrument and the methods developed to process its measurements. Exemplary measurements of both seawater and mineral deposits made during deployments of the device at an active hydrothermal vent field in the Okinawa trough are presented. Through integration with platforms such as underwater vehicles, drilling systems and subsea observatories, it is hoped that this technology can contribute to more efficient scientific surveys of the deep-sea environment.

1. Introduction

The application of manned submersibles and remotely operated vehicles (ROVs) to sampling has led to great advances in our understanding of deep-sea geochemical processes, since they allow for accurately geo-referenced chemical information to be obtained from samples whose origins and context are known. However, the number of samples that can be retrieved limits the range and spatial resolution of the information obtained, and the information is not immediately available for feedback since the analysis is typically performed in a laboratory. Recent advances in measurement technology and vehicle infrastructure have seen the successful application of in situ sensors whose measurements can increase the spatial and temporal resolution of chemical information, and enable informed decisions to be made based on real-time data (Okamura et al., 2001; Fukuba et al., 2009; Luther et al., 2001; Nuzzio et al., 2002; Provin et al., 2013). Most of these techniques, however, are limited to measurement of a single target element or molecule that is dissolved in seawater. On the other hand, spectroscopy is rapidly emerging as a versatile tool that can expand the envelope of modern oceanographic sensors. Spectroscopy allows for non-contact multivariate analysis, with a large variety of interactions that can be applied to probe different aspects of the deep-sea environment. Laser Raman (LR), a technique based on non-linear scattering of light, has been used to study the molecular chemistry of gases dissolved in seawater and also measure the composition of gas hydrate complexes at depths of up to 3600 m using a deep-sea LR probe developed by the Monterey Bay Aquarium Research Institute (MBARI) (Brewer et al., 2004; Zhang et al., 2010). In this paper, we describe the development of a 3000 m depth rated Laser-induced breakdown spectrometer and its deployment from a ROV at a deep-sea hydrothermal vent field in the Okinawa trough. The

* Corresponding author. Tel.: +81 30 5452 6487.
E-mail address: blair@iis.u-tokyo.ac.jp (B. Thornton).

http://dx.doi.org/10.1016/j.dsr.2014.10.006

instrument is capable of measuring the elemental chemical composition of both fluids and solid deposits, and so can be used to study different aspects of deep-sea geochemistry compared to the LR technique, which is effective for looking at molecular chemistry. The requirements to obtain high quality signals underwater and at oceanic pressures using laser-induced breakdown spectroscopy (LIBS) are described and we discuss the engineering developments that were necessary to make the instrument field operational. The results of controlled laboratory experiments are presented together with data processing techniques that have been developed to interpret the signals in a scientifically useful way. Spectra obtained during deployments at sea demonstrate the unique ability of the instrument to perform in situ, multi-element chemical analysis of seawater and mineral deposits at depths of over 1000 m. Finally we discuss directions for future developments regarding instrumentation and signal processing methods and describe potential application areas for the device.

2. Underwater LIBS at high pressure

LIBS is a form of atomic emission spectroscopy (AES) that focuses a high power laser-pulse to generate a plume of excited material. The excited material, or plasma, emits specific wavelengths of light that correspond to the atoms and ions that compose the plume. The method can, in principle, detect all elements if sufficiently high excitation temperatures can be achieved (Miziolek et al., 2006). An advantage of this method is that it allows for real-time analysis of gases, liquids and solids with no requirement for sample preparation, making it an attractive technique for in situ analysis. LIBS can probe different aspects of the deep-sea chemical environment compared to the LR technique, since it measures elemental, not molecular, composition. The two methods are essentially complementary, however, while not all materials are Raman active, LIBS can in theory measure the composition of any target since all matter is composed of elements. The advantages of LIBS for in situ analysis has been recognized by several groups and it has found application in the field for environmental soil monitoring (Wainner et al., 2001; Harmon et al., 2005; Yamamoto et al., 1996; Mosier-Boss et al., 2002), survey of nuclear power plants (Whitehouse et al., 2001; Saeki et al., 2014) and recently planetary exploration (Wiens et al., 2002, 2012; Maurice et al., 2012; Meslin et al., 2013).

Studies of underwater LIBS however, often report strong confinement and plasma quenching effects due to the nearly incompressible fluid medium, which can significantly degrade the quality of the signals obtained. The interactions within the optically dense plasmas generated underwater are far from ideal for spectroscopy (Sakka et al., 2002; Pichahchy et al., 1997). In order to overcome this problem, most studies concerning underwater LIBS have used a double-pulse technique (Nyga and Neu, 1993; De Giacomo et al., 2005; Lazic et al., 2005, 2007), where a first pulse is used to create a cavity into which a second pulse is delivered, allowing mechanisms similar to LIBS in a gas to take place. However, several studies have reported that this method is sensitive to external pressure, with pressures of just a few MPa, corresponding to depths of a few hundreds of meters, having a significant detrimental effect on the analytical value of the signals obtained (Lawrence-Snyder et al., 2007; Michel and Chave, 2008b; De Giacomo et al., 2011; Takahashi et al., 2013). This had ruled out the possibility of applying LIBS to in situ chemical analysis in high-pressure liquid environments such as the deep-sea. However, studies at the Woods Hole Oceanographic Institution demonstrated for the first time, that with an appropriate setup, narrow spectral lines can be observed from plasmas generated directly in bulk ionic solutions at high pressures of up to 30 MPa using a conventional single-pulse (Michel et al., 2007; Michel and Chave, 2008a). Similar results have also been reported independently by our group (Masamura et al., 2011) and the Ocean University of China (Hou et al., 2014). In Thornton and Ura (2011), the authors further demonstrated that narrow spectra can be observed from water immersed solids using a single-pulse with no significant effect of pressure up to 30 MPa. The difference in behavior observed for the single and double-pulse methods at high hydrostatic pressures has been linked to the transient pressure shockwaves generated when a high power laser-pulse is focused in a nearly incompressible medium such as water (Thornton et al., 2012a, 2013, 2014a). Based on these findings, we developed a prototype In situ Seafloor Element Analyzer (I-SEA), which is capable of both single and double-pulse LIBS measurements. The system was deployed in the Kagoshima bay at a depth of 200 m during March 2012 (Thornton et al., 2012b). During the experiment, the instrument was deployed from an ROV and measurements were performed using a single pulse. Successful measurements of seawater composition were achieved. While emission spectra were also observed from solid test pieces mounted on the ROV, the quality of the signals obtained was poor compared to controlled laboratory experiments performed using the same specimens underwater at the same hydrostatic pressure. The difference in quality was attributed to difficulty in focusing the instrument on a solid surface using a ROV manipulator, combined with the sensitivity of underwater measurements using a conventional single-pulse to surface roughness.

The next major development took place when it was demonstrated that the long-pulse laser excitation technique, which uses a single-pulse of duration $\sim$150 ns (Sakka et al., 2006, 2009, 2014), can offer significant enhancements in signal quality compared to a conventional single-pulse (with pulse durations of <20 ns) for both solids immersed in water (Thornton et al., 2013) and also bulk ionic solutions (Thornton et al., 2014a). In both cases, no significant degradation in signal quality was seen for external pressures up to 30 MPa. While the authors are presently investigating techniques to further optimize LIBS measurements in high pressure underwater environments, our present setup using the long-pulse technique has detection limits in the order of tens of μmol/kg for certain species in dissolved ionic solutions and in the range of 0.1–1.0 wt% for certain elements in seawater immersed solids. These limits are sufficient for detection of several major elements in seawater and hydrothermal fluids (Kennish, 2000; Kawagucci et al., 2011) and mineral deposits (Ueno et al., 2003) found in volcanically active areas of the seafloor. Based on these studies, we have developed our 2nd generation LIBS device, called the ChemiCam (Chemical Camera), that incorporates a long-pulse laser and addresses several of the issues identified through operation of I-SEA. It should be noted that while the name of the device is similar to the Los Alamos National Laboratory's ChemCam (Maurice et al., 2012), deployed on the Mars Science Laboratory (MSL) rover Curiosity, the devices are unrelated and their developments have been independent of each other. The jump from laboratory demonstration to field deployment of ChemiCam has not been trivial. While the prototype I-SEA was built using commercially available lasers and spectrometers, the components of ChemiCam are almost entirely custom made. In particular, the specifications of the long-pulse laser used in the laboratory experiments (Sakka et al., 2006, 2009, 2014; Thornton et al., 2013, 2014a) are not met by any commercially available laser and a significant investment of effort was required to develop a robust, compact long-pulse laser that can be incorporated into a field deployable LIBS instrument. While the application of a long-pulse laser is seen as the key technology for the realization of deep-sea LIBS, a number of other technical issues have also been overcome and are described in the next section.

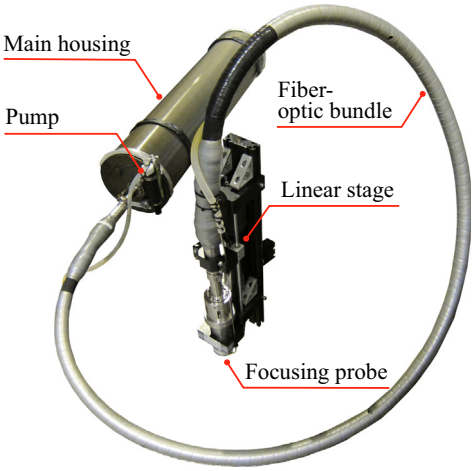

Fig. 1. The 3000 m depth rated LIBS device ChemiCam.

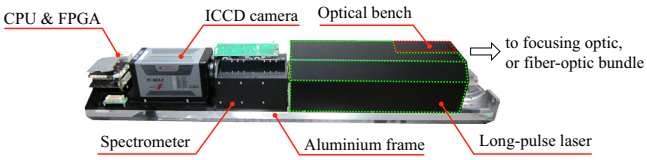

Fig. 2. Configuration inside the main housing.

3. Instrument

ChemiCam is a 3000 m depth rated LIBS device that has been developed by the University of Tokyo, Japan. The device has the unique ability to perform in situ multi-element chemical analysis of both liquids and mineral deposits in the ocean at depths of up to 3000 m. The device, shown in Fig. 1, is 1.3 m long with a diameter of 0.3 m and weighs 160 kg in air. The main housing contains a custom made long-pulse laser capable of delivering a maximum pulse energy of 40 mJ at a repetition rate of 1 Hz. The duration of the pulse can be controlled between 150 and 250 ns. The optical emissions of the laser-generated plasmas are observed using an intensified charged coupled device (ICCD) camera and a spectrometer. The device contains a single board central processing unit (CPU) that controls the laser, communicates with the ICCD camera and stores the spectral measurement data. Synchronization of the various components is achieved using a custom made field-programmable gate array (FPGA). All components are arranged along a rigid aluminum frame, shown in Fig. 2, which fits inside the instrument's main housing. The necessary voltage convertors and power distribution electronics are fixed directly to the aluminum frame to allow heat to disperse through the main housing. Power supply, instrument control and signal telemetry are provided through a ROV tether. Communication is achieved through a single serial connection or, if available, an Ethernet connection and the system is powered using a single 100 VAC supply.

The instrument has two modes of operation. In the first mode, the laser is focused directly via a lens mounted on the lid of the main housing and spectroscopic measurements of seawater composition are made. In this mode, a conductivity and temperature (CT) sensor can be attached as a peripheral device and its measurements logged by the main CPU. In the second mode, the laser is fired through a 4 m fiber-optic cable and is focused via an optical head that can be held by a ROV manipulator. This setup is used to make spectroscopic measurements of mineral deposits. In this mode, the CPU sends commands to a control a linear stage and pump, which are attached as peripheral devices. Table 1 shows the general specification of the device in each mode of operation.

Table 1
General specification of ChemiCam.

Physical and electrical information		
Length (main housing) [m]	1.3	
Diameter [m]	0.3	
Maximum depth [m]	3000	
Operational mode	Mode 1	Mode 2
Measurement target	Dissolved ions	Mineral deposits
Weight in air [kg]	140	160
Weight in water [kg]	25	40
Power consumption [W]	130	140
Peripherals	CT sensor	Pump Linear stage
Power supply [VAC]	100	
Communication	RS232 or Ethernet	
Optical characteristics		
Focusing method	Direct	Optical head via 4 m fiber
Focusing optic	10 × Objective lens	5 × Cassegrain
Laser type	Q-switched DPSSL Nd:YAG	
Pulse energy (at target) [mJ]	30	20
Pulse duration [ns]	150 to 250	150 to 250
Laser wavelength [nm]	1064	
Spectrometer type	Czerny-Turner	
Inlet slit dimensions [mm]	0.5 × 8	
Spectral range [nm]	400 to 800	295 to 550
Spectral resolution [nm]	1.6	0.8
Detector type	ICCD (Gen. III)	
Number of pixels	1024 × 256 (i.e. 1024 ch)	

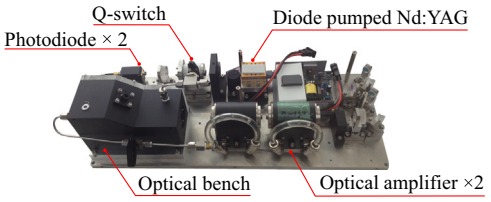

Fig. 3. Long-pulse laser developed for ChemiCam.

3.1. Long-pulse laser

The greatest challenge in realizing a deep-sea LIBS instrument was the development of a long-pulse laser that is compact and robust enough to be applied at sea. Fig. 3 shows the long-pulse laser developed for ChemiCam, where most of the electronic components built into the laser have been removed in the photo for clarity. The laser is a Q-switched Nd:YAG diode pumped solid state laser (DPSSL) that operates at its primary wavelength, i.e. 1064 nm. Although the chosen wavelength is strongly absorbed by water, the high power output that can be achieved for Nd:YAG lasers operating at this wavelength outweigh the effects of absorption in water for measurements at short range. In our system, the laser travels through 4 mm water and so over 85% of the lasers energy reaches the target (Morel, 1974). While measurements at a longer range may favor the use of visible wavelength lasers, it must be considered that the wide range of wavelengths emitted by the plasmas generated are also absorbed by seawater and will tend to become limited to just the visible band. All the necessary optical and electronic components of the laser are mounted on a rigid 50 by 20 cm base plate. The laser cavity has a length of 1.8 m, which was found to be necessary to generate the required length of pulse, i.e. >150 ns. A total of 9 mirrors are used along the laser cavity to keep the external dimensions of the laser as compact as possible. The laser-pulse directly generated by the

cavity does not have sufficient energy to generate plasmas and so two optical amplifiers are used to achieve the necessary pulse energy. The laser has two analogue control inputs that can be used to control the duration of the pulse between 150 and 250 ns and the pulse energy via the main CPU, where maximum pulse energy that can be delivered by the system is 40 mJ. Based on experimental studies, we have determined the breakdown thresholds of seawater-immersed solids using this laser to be in the region of 0.5 to 1 GW/cm^2 for various different sediment and rock samples. These are lower than the breakdown thresholds determined for bulk seawater, which are in the region of 5 to 10 GW/cm^2 depending on impurities, as has previously been reported for ns-duration pulse lasers at 1064 nm (Kennedy et al., 1995, 1997). Since there is a significant difference in the required thresholds for breakdown to occur, different settings are necessary for measurements of seawater and immersed solids, respectively. The laser has two photodiodes that monitor the laser-pulse characteristics. The first photodiode is used as an optical trigger to synchronize the measurements of the detector. The second photodiode is connected to a 20 MHz analogue-to-digital convertor that is used to measure the profile of the laser-pulses being fired. This allows both the pulse power and pulse duration to be monitored during operation. All the necessary laser parameters can be controlled and monitored through a custom-made software package and information concerning these settings and the measured characteristics of the laser-pulse are stored for each measurement made by the device.

3.2. Spectrometer and detector

Plasmas generated underwater usually emit light for no longer than 2 or 3 μs, where the first 0.3 to 0.5 μs is typically dominated by an intense continuum of light that does not contain any element specific information. In order to perform elemental analysis underwater and at high pressure, it is necessary to use a detector that can be synchronized to the laser with an accuracy of a few tens of ns and can be gated to capture the element specific line emissions that occur after the continuum subsides. For this, a gated ICCD camera (Princeton Instruments PiMAX 4 Gen. III) is used, where the observation time window can be controlled in single ns steps from the main CPU. The ICCD camera is synchronized using the optical trigger built into the laser as a reference. The spectra are stored by the devices main CPU and are also displayed in real-time through the ROV tether to provide feedback to the instrument's operator.

The optical emissions of the plasmas generated by the long-pulse laser are observed through a 12 cm focal length, custom-built Czerny–Turner spectrometer. Light enters the spectrometer through a bundle of 40 100-μm-core diameter optical fibers that are aligned vertically along a 50 μm slit with a height of 8 mm. The light throughput of the spectrometer (*f*/4.5) is optimized to match the numerical aperture (NA) of the optical fibers (NA=0.11). Different gratings are used for measurements of solids and liquids. For liquids, a 300 groove/mm grating is used to measure the spectrum between 400 and 800 nm with a resolution of 1.6 nm. For solids, a 600 groove/mm grating is used to measure the spectrum between 295 and 550 nm with a resolution of 0.8 nm. The reason for the different setups is that the emission lines of the major elements dissolved in seawater are sparse and span a wide range of wavelengths, whereas solids typically have more complex matrices and require a higher resolution to resolve adjacent lines. Shorter wavelengths also contain more information regarding transition metals (Kramida et al., 2013), which are of interest when measuring mineral deposits. The range and resolution of the measurements was chosen based on the results of preliminary studies using standard seawater samples and massive sulfide deposits, while also taking into consideration the sensitivity of the detector and optical setup used. While higher spectral resolution can be achieved using Echelle type spectrometers (Michel et al., 2007), these typically have a much lower light throughput (*f*/7–*f*/10) and require a slit with an aspect ratio close to 1 (e.g. 50 × 50 μm), which limits the amount of light that can enter spectrometer. Since emission lifetimes for measurements made underwater are short, the present spectrometer was designed to maximize the overall sensitivity, i.e. a high light throughput and a large area slit. With regards to the detector, while higher levels of sensitivity can be achieved using photon multiplier tubes (Cremers et al., 1984), this comes at the cost of resolution since measurements are limited to just a few wavelength channels.

3.3. Optical setup

While the laser, spectrometer and detector used for measurements of solids and liquids are essentially the same, the optical setups used to focus the laser and observe the optical emissions are different. In both cases, the optical setups are designed to achieve efficient delivery of the laser's energy without damaging the optical components, while also being able handle the broad range of wavelengths observed during spectroscopic measurements. The latter point presents a significant challenge since the refractive index of fused-silica-glass, used in most lenses, is wavelength dependent and changes significantly for wavelengths <480 nm (Malitson, 1965).

3.3.1. Analysis of liquids

The optical bench used for measurement of liquids is shown in Fig. 4. The bench consists of a 5 × magnification beam-expander, two right-angle mirrors, a dichroic mirror, a parabolic mirror and a fiber-optic bundle. Light from the laser, shown in green in the figure, first passes through the 5 × magnification beam-expander in order to reduce the risk of damage to the remaining optical components. Two right angle mirrors are used to align the laser along the central axis of the device. The dichroic mirror transmits the 1064 nm wavelength of the laser, which is focused using a 10 × magnification standoff objective lens with a working distance of 30 mm. The light passes through a curved silica-glass pressure-tight window of wall thickness 13 mm that is fixed to the end cap of the main pressure housing, shown in Fig. 5. The pressure window is designed so that both its faces are spherical with their centers of curvature located at the focal point of the objective lens. Since all light passes through the window at zero angle of incidence, no refraction occurs at either face and so all wavelengths are focused onto the same point in space (Thornton et al., 2014b). The light from the laser is focused down to a spot of diameter <50 μm, 4 mm from the water-exposed surface of the pressure window. The intensity of the laser at the focal point is sufficient to cause breakdown in bulk liquids. The light from the plasma, shown in red in Fig. 4, is observed along the same optical path used for laser delivery. Light from the plasma passes through the con-focal pressure window with a zero angle of incidence,

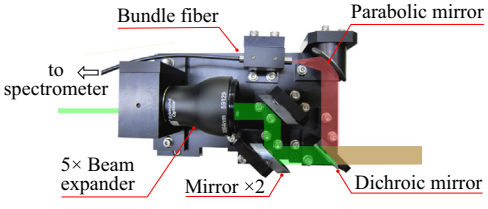

Fig. 4. Optical bench for measurement of liquids. The path of the laser is shown in green and light from the plasma follows the path shown in red. (For interpretation of the references to color in this figure legend, the reader is referred to the web version of this article.)

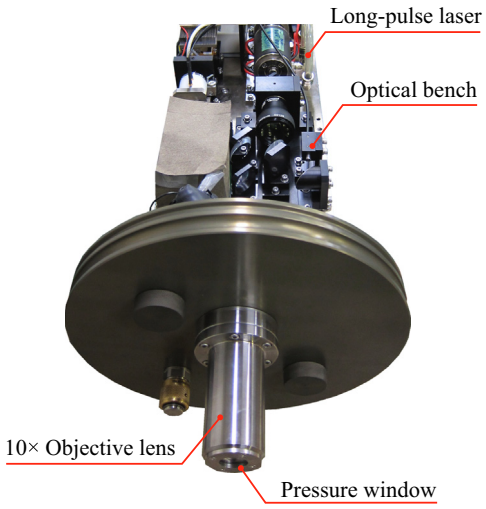

Fig. 5. Setup for measurement of liquids. Light is focused into a bulk liquid using a 10× magnification objective lens with a 3000 m depth rated zero-refraction pressure window.

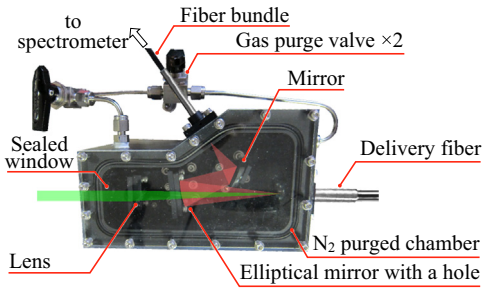

Fig. 6. Optical bench for measurement of solids. The path of the laser-pulse is shown in green, and light from the plasma is observed along the red path. (For interpretation of the references to color in this figure legend, the reader is referred to the web version of this article.)

allowing a broad range of wavelengths to be efficiently observed without any chromatic aberration. Light from the plasma is then collimated by the same objective lens used for laser delivery, which can compensate for chromatic effects between 480 and 1800 nm. The collimated plasma emissions of wavelengths between 400 and 800 nm, which are used for spectroscopy, are reflected by the dichroic mirror and are focused into a bundle of 40 100-µm-core diameter fibers using a parabolic mirror. The other end of the bundle connects directly to the inlet of the spectrometer.

The con-focal pressure window and parabolic mirror to guide light from the plasma into the observation fiber do not suffer from chromatic effects. However, there is some loss in efficiency for wavelengths <480 nm due to chromatic aberration of the objective lens used to collimate the plasma emissions. In order to account for these effects and calibrate the instrument, the wavelength dependent observation efficiency of the system is measured between 400 and 800 nm as described in Section 3.4.

3.3.2. *Analysis of solids*

Measurements of solid deposits require precise focusing of the optics onto the target's surface. In order to achieve this, a 4 m long fiber-optic cable is used to deliver the laser-pulse to a compact focusing optic that can be manipulated by the ROV. The ROV manipulator is used to bring the probe near the measurement target and a single-axis linear stage is used to focus the laser and observation optics onto its surface. The optical bench used for this

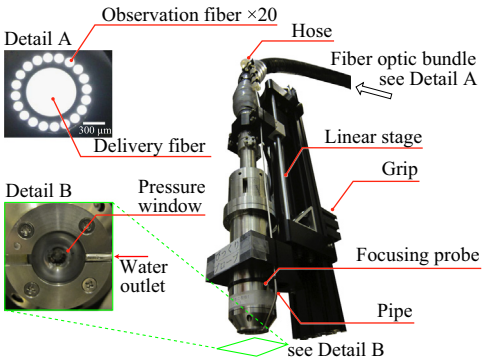

Fig. 7. Focusing probe used to focus the laser and observation optics onto solid surfaces. The linear stage is controlled using ChemiCam's CPU to adjust the distance to the target. The 3000 m depth rated probe contains a 5× magnification Cassegrain reflection-optic to focus light onto the target's surface. Detail A shows the cross-section of the fiber optic bundle that passes through the focusing probe. Detail B shows the outlet of the seawater pump that is used to prevent turbid build up between the pressure window and the focal point of the laser.

setup, shown in Fig. 6, consists of a nitrogen gas purged chamber that contains a lens and two mirrors to guide light from the laser and plasma.

The laser-pulse enters the unit from the left side of Fig. 6 via a sealed fused-silica-glass window and is focused into a delivery fiber using a 100 mm focal length lens. The light passes through a 2 mm diameter hole in the elliptic mirror located between the lens and the fiber and enters the 600 µm-core diameter fiber (NA=0.11) that delivers the pulse to the target. The end of the fiber is sealed and mounted on a XY stage so that it can be aligned with the laser. The fiber penetrates the end cap of the main pressure housing and enters the focusing probe using 3000 m depth rated fiber-optic penetrator units developed by Ocean Cable Co. Ltd. for this application. The reason for using penetrators is to minimize losses in the system and eliminate the risk of damage to any connecting parts due to the high intensity of the laser. The fiber-optic bundle that penetrates the housings is cased in a 2 mm internal diameter pressure tight stainless steel pipe, which maintains enough flexibility for manipulation.

The focusing unit, shown in Fig. 7, contains a 5× magnification Cassegrain reflection-optic and the spherical faced con-focal pressure window described previously. The housing of the focusing unit has an external diameter of 7 cm and is 50 cm long. Light from the laser is focused down to a spot size of 120 µm, 4 mm from the water-exposed surface of the pressure window. This provides sufficient intensity to generate a plasma on an immersed solid surface, but not directly in a bulk liquid. Light from the generated plasma is observed through the same optical path used for laser delivery. This allows the plasma to be observed normal to the target's surface and so maximizes the visible cross section. Although the refractive index of glass changes significantly over the observed range of wavelengths (Malitson, 1965), i.e. between 295 and 550 nm, efficient observation can be achieved since light from the plasma passes through con-focal pressure window at a zero angle of incidence and all wavelengths follow the same path through the Cassegrain reflection-optic. While a significant proportion of the light is observed via the delivery fiber, expansion of the generated plasma means that the region from which light can be observed is larger than the laser spot size (Thornton et al., 2012a, 2014a). In order to increase sensitivity, 20 100-µm-core diameter observation fibers are placed around the delivery fiber to observe light from the expanded region. The other end of these fibers pass through the penetrator units and lead directly to the spectrometer in the main pressure housing. The light that passes through the delivery fiber enters the optical bench in the main

pressure housing and is coupled into a bundle of 20 100-μm-core diameter fibers. Both bundles (i.e. a total of 40 100-μm fibers) are arranged vertically along the inlet slit of the spectrometer. Our experiments have shown that this arrangement increases the observational efficiency of the system by about 30% compared to when only light that passes through the delivery fiber is observed.

One of the challenges encountered during the sea trials of the 1st generation I-SEA device was the difficulty in focusing the laser onto a surface using the ROV manipulator. In order to address this issue, the present system has a single-axis linear stage that can be manually controlled from the main CPU. The linear stage has a stroke length of 20 cm and can be controlled in steps of 10 μm, where the maximum speed of the stage is 2 cm/s. During operation, the linear stage is held by the ROV manipulator and brought to within 20 cm of the measurement target. The linear stage is then used to control the distance between the focusing probe and target to make measurements. Another issue encountered during testing of I-SEA was increased turbidity near focal region of the laser due to build up of material ablated by the laser. To address this issue, an impeller is used to pump seawater from around the main pressure housing to the focal region of the laser using a hose that runs along the fiber-optic bundle. A stainless steel pipe on the end of the hose guides the flow to the region in front of the focusing lens, as can be seen in Fig. 7. The pump is also controlled by the instrument's main CPU. Finally, it is noted that the long-pulse used in ChemiCam is significantly more robust to surface roughness conditions compared to the conventional, short-duration (<20 ns) single-pulse used in I-SEA for measurements at depth.

3.4. Instrument calibration

In order to analyze the spectra measured by the system, calibration of the observation wavelength range and the wavelength dependent transmission efficiency of the system are necessary for both optical setups. Wavelength calibration is performed for each optical setup using a Mercury-Argon calibration source (Ocean Optics HG-1). The wavelength dependent transmission efficiency is determined for both setups using a Deuterium-Tungsten Halogen calibration light source (Ocean Optics DH-2000-CAL), where both light sources cover the entire spectral range observed using ChemiCam. For transmission efficiency calibration, the light source is coupled to a fiber and the opposite end of the fiber is placed at the focal point of the laser. The wavelength dependent attenuation properties of seawater can be compensated using coefficients for clear seawater (Morel, 1974). While this procedure does not take into account the wavelength dependent attenuation of suspended particulate matter, these effects are mainly associated with phytoplankton in shallow coastal waters (Kirk, 1983, 1994) and organic detritus (Prieur and Sathyendranath., 1981) and are not expected to be significant for deep-sea applications where light from the plasma travels through only 4 mm of seawater. All spectra shown in this paper have been corrected based on the intensity calibration of each setup that was used.

4. Signal interpretation

This section describes methods to extract information from underwater LIBS signals measured from artificial seawater and hydrothermal fluid samples and also seafloor sediment and rock samples that are representative of the different matrices present on the seafloor in the North West (NW) Pacific. Methods to interpret LIBS measurements can be broadly divided into three categories: classical calibration-curve-based methods, calibration-free methods and multivariate regression-modeling techniques. As with all forms of AES, the intensity of a LIBS signal is dependent not only on the concentration of each element in the target, but also on the target's matrix. Therefore the application of classical calibration-curves typically requires matrix-matched calibration standards (Miziolek et al., 2006; Eppler et al., 1996). However, the generation of comprehensive matrix-matched calibration-curves is not practical for field applications that investigate natural targets. Calibration-free (CF) methods provide a more general framework for quantification without the need for calibration-curves by accounting for matrix effects theoretically. This is achieved by applying the Boltzmann distribution law (Tognoni et al., 2010, 2007; Ciucci et al., 1999; Praher et al., 2010; Sallè et al., 2006), which assumes optically thin plasmas that are in local thermal equilibrium (LTE), to signals that contain peaks of all major elements in the target. Recently, multivariate analysis techniques have been applied to account for matrix bias through regression modeling of the spectra observed from samples of known composition. It has been demonstrated that, provided the data used to generate the models is sufficiently rich in information, the relationships determined by the models can be used to analyze unknown samples (Clegg et al., 2009; Meslin et al., 2013; Wiens et al., 2013). While there exists a significant body of literature regarding the interpretation of LIBS signals, investigation into whether these methods can be applied to measurements made underwater at oceanic pressures have only just begun.

4.1. Seawater

With regard to measurements of bulk ionic solutions, Cremers et al. (1984), Michel et al. (2007) and Masamura et al. (2011) generated calibration-curves that can be used to quantify measurements for single salts dissolved in pure water. The sensitivity of the measurements was found to vary between different elements and also vary between different peaks of the same element. Detection limits in the region of 10 to 250 μmol/kg were achieved for Group I and Group II elements, whereas the detection limits for transition metal elements were in the region of 5 to 50 mmol/kg (Cremers et al., 1984; Michel et al., 2007; Hou et al., 2014). While higher sensitivity has been demonstrated for measurements of water surfaces, droplets or films (Fichet et al., 2001, 2003; Arca et al., 1997; Samek et al., 2000; Wachter and Cremers, 1987; Huang et al., 2004; Lo and Cheung, 2002; St-Onge et al., 2004), these methods are not applicable since the application considered here requires measurement of bulk liquids.

Table 2 compares the concentration of dissolved metallic ions in seawater to hydrothermal vent fluids from the South Big

Table 2
Composition of seawater (Kennish, 2000) and hydrothermal vent fluids (Kawagucci et al., 2011) in the Iheya North hydrothermal vent field.

Vent site	Temp °C	Na mmol/kg	K mmol/kg	Ca mmol/kg	Mg mmol/kg	B μmol/kg	Sr μmol/kg	Li μmol/kg	Mn μmol/kg
SBC	153	185	26.9	4.6	–	670	9.4	355	–
NBC	304	434	72.3	16.1	–	1740	61.4	1225	619
HRV	189	466	79.2	20.5	–	2270	75.0	1362	678
CBC	86	363	66.8	17.0	–	1980	60.5	1132	535
Seawater	–	468	10.2	10.3	53.2	416	90.0	25	0.0005

Chimney (SBC), North Big Chimney (NBC), High Radioactivity Vent (HRV) and Central Big Chimney (CBC) in the Iheya North field, located as shown in Fig. 8, in the Okinawa trough (Kennish, 2000; Kawagucci et al., 2011). The samples cover a broad range of concentrations and are representative of the range of concentrations of oceanic fluids in the NW Pacific. Other metallic ions, such as Fe, Zn, Cu, are typically only contained in trace quantities in this region. The dissolved ions of Li and K are enriched in the hydrothermal fluids, whereas Sr and Mg are both depleted. Na and Ca also show sufficient contrast in concentration compared to seawater to expect discrimination by LIBS. While Mn and B also show contrast in concentration between the different samples, the levels of concentrations are significantly smaller than the detection limits reported for transition metals and metalloids in bulk fluids (Cremers et al., 1984; Hou et al., 2014). Fig. 9A–D shows the spectra obtained from artificial solutions that match the dissolved metallic ion content of the fluids in Table 2. The spectrum of artificial seawater is shown in each plot as a dotted line for comparison. The solutions were made by dissolving NaCl, $MnSO_4 \cdot 5H_2O$, $CaCl_2$, KCl, $Li_2SO_4 \cdot H_2O$, H_3BO_3, $SrCl_2 \cdot 6H_2O$ and $MgSO_4 \cdot 7H_2O$ in pure water (Milli-Q). It should be noted that while the metallic content has been matched, the non-metallic components may well differ from the actual oceanic fluids. Measurements were performed at room temperature and at atmospheric pressure, where a single 30 mJ pulse (energy at the target) of duration 250 ns was used. The observation gate delay and width were set to 1200 ns from the rising edge of the pulse and 1000 ns, respectively, where a relatively long delay was chosen to avoid the unstable and highly variable emissions of H at 486.1 and 656.2 nm and O at 777.2 nm that were found to occur for delays < 1000 ns using this setup. The spectra shown are the average of 10 measurements that have been normalized by the total integrated intensity after subtraction of the background. While not all the observed peaks have been identified, Ca at 422.6 nm, Mg at 517.3 and 518.3 nm, Na at 588.9 and 589.5 nm, Li at 670.8 nm and K at 766.4 and 769.8 nm can be clearly seen in the spectra. The concentrations of Ca, Li and K relative to Na increase in the order of SBC, NBC, HRV and CBC (A to D). It can be seen that the Li and K lines are significantly stronger for the four hydrothermal samples than for seawater. The Mg line is only visible in the seawater sample, since Mg is depleted in the pure hydrothermal fluids (Kawagucci et al., 2011) on which our samples are based.

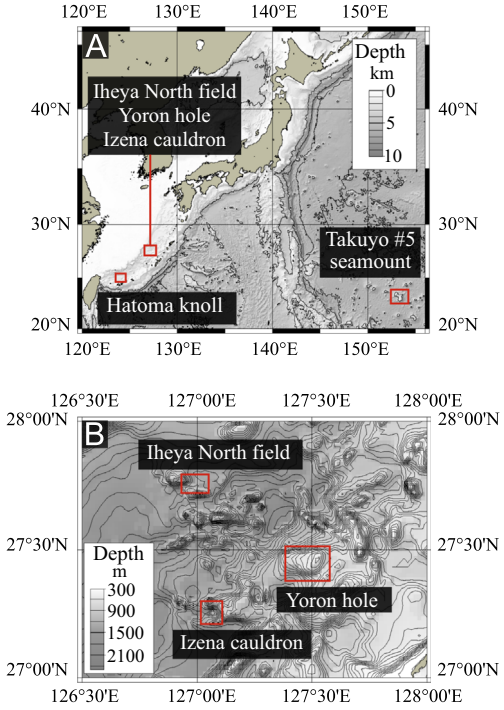

Fig. 8. (A) Locations from where the samples used in the laboratory experiments were obtained, and (B) a more detailed bathymetric map showing the locations of the Iheya North field, Yoron hole and the Izena cauldron hydrothermal vent areas. The sea trials were performed in the Iheya North Field.

Under the assumption of an optically thin plasma satisfying LTE, the intensity of the spectral emissions can be related to the abundance of each element in the plasma, N_s, using the Boltzmann distribution law,

$$N_s = \frac{I_{sij}}{F} \times \frac{U_s(T)}{A_{sij} g_{si} e^{-E_{si}/kT}}, \quad (1)$$

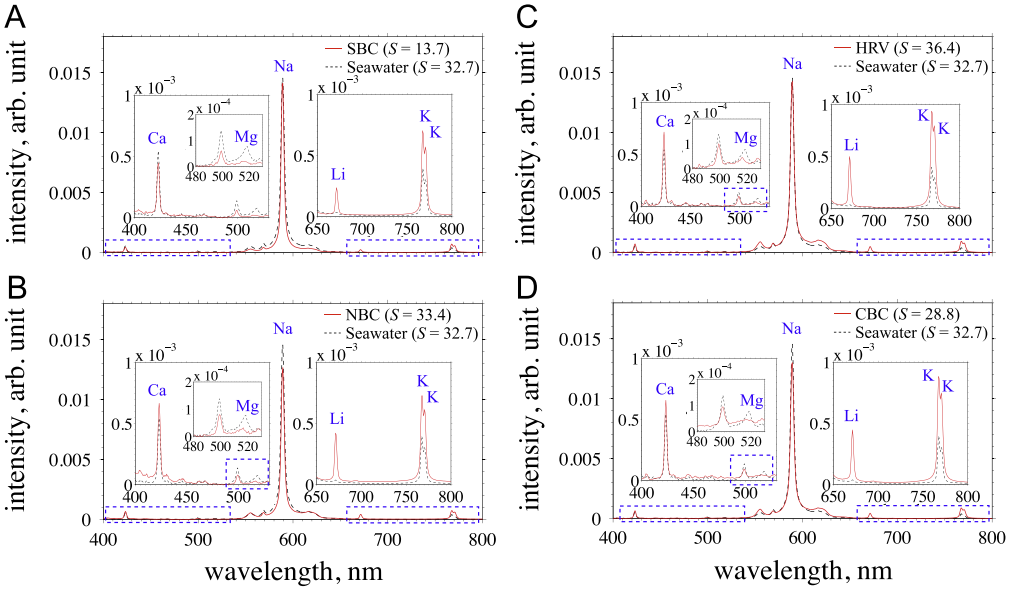

Fig. 9. Spectra of bulk fluids based on the composition of (A) SBC, (B) NBC, (C) HRV and (D) CBC vent fluids. The spectrum obtained from seawater is shown by the dotted line in each plot for comparison. The concentration of metallic ions is given in Table 2. The salinity of each sample measured using a CT sensor is noted in top right corner of each plot.

where $I_{s\ ij}$ is the intensity of the peak, $A_{s\ ij}$ is the transition probability, $g_{s\ i}$ is the degeneracy factor, $E_{s\ i}$ is the excitation energy, k is the Boltzmann constant and $U_s(T)$ is the partition function of each species at the electron excitation temperature T. The subscripts i and j indicate the upper and lower energy level of the element s. The parameters $A_{s\ ij}$, $g_{s\ i}$, $E_{s\ i}$ and $U_s(T)$ can be obtained from the National Institute of Standards and Technology (NIST) database (Kramida et al., 2013) and Atomic spectral line database (Smith et al., 2014). The parameter F accounts for the wavelength dependent optical efficiency of the observation system and the plasma's volume and density. The latter two components of F relate to the measurement setup and normally do not need to be considered when generating calibration-curves or performing CF-LIBS calculations since they are neither wavelengths nor element dependent. It can be seen from Eq. (1) that the strength of the signal is both element and wavelength dependent and also requires the electron excitation temperature to be known. Studies that use classical calibration-curves essentially make the assumption of a fixed plasma temperature, which simplifies the relation into a linear correlation between peak intensity and relative abundance, C_s, of each corresponding element as follows,

$$N_s \propto C_s = w_{s\ ij} I_{s\ ij}. \tag{2}$$

The parameter $w_{s\ ij}$ is an experimentally determined weighting factor, whose value is constant for each element specific peak. While the assumption of a fixed plasma temperature introduces some uncertainty, it is still possible to generate linear calibration-curves that are useful for analysis of bulk fluids provided they have the same matrix (Cremers et al., 1984; Michel et al., 2007; Masamura et al., 2011). However, Michel et al. (2007) and Masamura et al. (2011) demonstrated that $w_{s\ ij}$ changes significantly for different sample matrices. While matrix-matched standards can in theory be used to quantify measurements of oceanic fluids, their application would require the matrix of the target to be known prior to the analysis, which is typically not the case for exploratory surveys.

CF-LIBS attempts to overcome these issues in two steps. First, the electron temperature T is determined by plotting a Boltzmann distribution curve using multiple peaks of the same element. By assuming LTE, the abundance of each element can be calculated by substituting the value of T determined from the plot into Eq. (1). In the second step the concentration, of each element can be calculated by applying the following condition,

$$C_s = \frac{N_s}{\sum N_s}, \text{ where } \sum N_s = 1. \tag{3}$$

The underlying concept behind CF calculations requires all major elements to be detected in the spectrum to quantify the results. While some groups have looked into CF methods for seawater analysis using inductively coupled plasma (ICP) AES (Tognoni et al., 2009), this method cannot be applied to the LIBS measurements of bulk fluids made in this work since non-metallic ions such as Cl, S, O, H, cannot be reliably detected over the range of wavelengths observed, despite the fact they compose almost 99 wt% of the fluids. In order to address this problem, we introduce salinity, S, as an external reference to bound the solution of Eq. (3). Salinity can be determined from CT measurements based on the Practical Salinity Scale (Perkin and Lewis, 1980; UNESCO, 1980). While the salinity determined from CT measurements does not have units, the measurements are still suitable for use as an external reference since they relate linearly to the total concentration of dissolved ions.

The salinity of each sample measured using a CT sensor (Infinity series, JFE Advantach Co. Ltd.) is noted in the legend of each plot in Fig. 9 where the standard deviation of the salinity measurements was <0.002 for all samples. Fig. 10 shows the salinity measurements of each sample plotted against the total concentration of dissolved Na, Ca, Mg and K, which account for >98 wt% of dissolved metallic ions in oceanic fluids (Kennish, 2000; Kawagucci et al., 2011; Ishibashi et al., 2014). The results show good linearity ($R^2=0.9987$) over the range of measurements made, suggesting that the total abundance of these major metallic ion, which can be detected in the LIBS signal, can be used as a proxy for S. Based on this proportional relation, we modify Eq. (3) as follows,

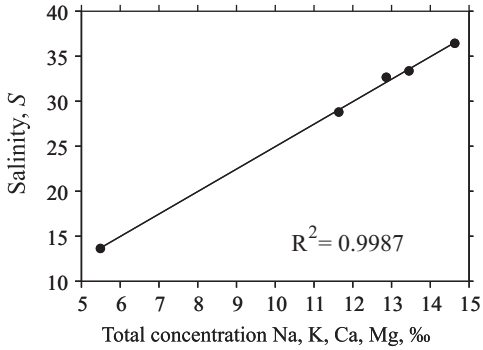

Fig. 10. Salinity measurements of a CT sensor plotted as a function of the total concentration of Na, Ca, Mg, and K, for the 5 samples on which laboratory studies were performed.

$$C_s \propto C_s' = \frac{w_{s\ ij} I_{s\ ij}}{\sum w_{s\ ij} I_{s\ ij}} S. \tag{4}$$

Eq. (4) compensates for the effects of the matrix on the overall intensity of the signals observed and also compensates for shot-to-shot variations in signal strength through use of the external reference, S. While this method requires independent measurements of S to be made, this is not limiting since calibrated CT measurements are standard on most scientific surveys. At the same time, this approach relaxes the requirement of CF-LIBS for all species to be detected in the spectrum, as it is sufficient to know just the relative abundance of the major metallic ions, i.e. Na, Ca, Mg and K, to quantify the results. While the method described borrows from the concept behind CF methods, it is not a CF method itself since it still requires calibration-curves to determine the concentration of each element from C_s'. The advantage over conventional calibration-curve based methods lies in its generality since quantification can be achieved using a single set of calibration-curves, without the need for matrix-matched standards.

The algorithm is applied to LIBS measurements of the artificial fluids shown in Fig. 9. The intensity of the peaks, $I_{s\ ij}$, are determined by considering the areas under a Lorentz curve fit of each peak as described in Sakka et al. (2009). Ideally, the method would be implemented directly based on Eq. (1) by determining T from a Boltzmann plot of a single element. However, the sparse signals observed from bulk fluids in this work consist of just a few peaks or doublets for each element and do not contain enough information to estimate T accurately (Miziolek et al., 2006; Aguilera and Arago, 2007). For the purpose of this study, a constant value of T is assumed. The values of $w_{s\ ij}$ are determined by applying Eq. (2) to the signals observed from the 5 artificial samples and taking the average value for each peak, which are used in all our calculations. Fig. 11A–D shows the calibration-curves generated for Na, Ca, K and Li, respectively, using the algorithm. The average and standard deviation of 100 sets of 10 accumulated signals for each sample are shown. The results show good linearity over the range of concentrations tested, with R^2 values of 0.9867, 0.9924, 0.9967 and 0.9973, for Ca, Na, K and Li, respectively. Ca had the lowest R^2 value and this is attributed to the poor sensitivity of the optical setup in this region of the spectrum (<480 nm). While the detection limits for the device

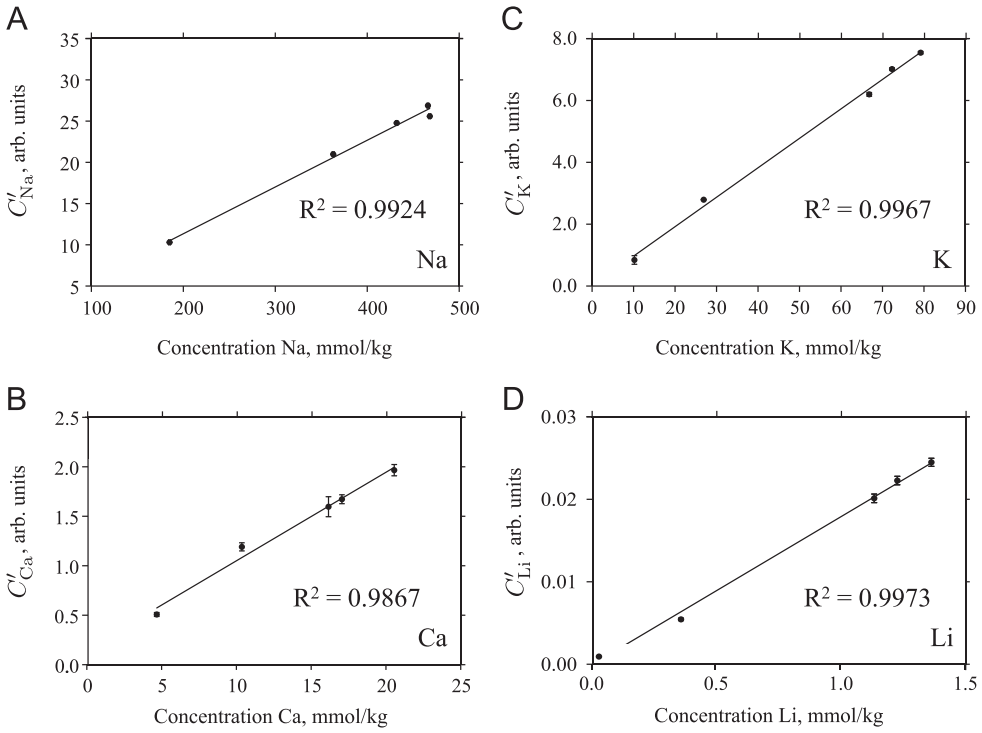

Fig. 11. Calibration-curves for (A) Na, (B) Ca, (C) K, and (D) Li.

have not been accurately established, the 25 μmol/kg of Li in seawater can be identified in the signals.

4.2. Sediments and rocks

Immersed solids typically have much richer spectral signatures than bulk liquids. While matrix-matched calibration-curves can be used for quantitative analysis of solids (Hunter and Piper, 2006; Eppler et al., 1996), various groups have successfully implemented CF-LIBS to quantify the composition of metal alloys (Tognoni et al., 2007, 2010; Ciucci et al., 1999; Herrera et al., 2009a) and metal oxides (Praher et al., 2010) in a gaseous environment, achieving relative accuracies of 5 to 15% for major elements. With regard to interpretation of natural sediments and rocks, most studies report degradation in accuracy due to the complexity of the signals obtained (Tognoni et al., 2010; Herrera et al., 2009b; Colao et al., 2004; De Giacomo et al., 2007). Moreover, conventional CF methods require all the major elements to be identified in the spectra, which is not possible for the limited range and resolution of the spectrometer used in ChemiCam. In situations where only a limited region of the spectrum can be observed, CF methods can still be used to determine the relative abundances of elemental species by normalizing against an internal standard (Sallè et al., 2006).

Multivariate analysis has been recently applied to account for matrix bias in situations where not all elements can be detected (Clegg et al., 2009). In this method, conventional calibration-curves are replaced by regression curves that model the entire observed spectra of samples with known compositions. Regression curves have the advantage that they can account for the effects of different matrices on the signals, where the key requirement is that the data used to train the regression models needs to be representative of the geological diversity expected during the surveys. It has been demonstrated that the composition of unknown samples, with a variety of matrices, can be determined with root-mean-square error products $< 10\%$ (Wiens et al., 2013). This method is currently used on the ChemCam instrument that was deployed on-board the MSL Rover Curiosity, where the pre-flight calibration data for signal interpretation consisted of 69 powder pellet rock standards and the system has been successfully applied to quantify LIBS spectra and study soil diversity at the Gale Crater on Mars (Meslin et al., 2013).

While the methods described show promise for quantitative analysis of targets with complex matrices, it has not yet been investigated whether these techniques can be used for rocks and sediments immersed in seawater that are measured using a single long-pulse. In Takahashi et al. (2014), the authors applied CF-LIBS to quantify long-pulse measurements of water immersed brass alloys with error products of $< 10\%$. While this demonstrates that LIBS signals obtained using this method are suitable for quantitative analysis, further work is necessary to extend our capabilities to quantify natural rock and mineral samples. For now, we apply CF-LIBS calculations using internal calibration methods to determine the relative abundances of Zn–Pb–Cu, which can be used to evaluate different types of hydrothermal deposit.

Table 3 shows the composition of seafloor sediment and rock samples, obtained from the locations shown in Fig. 8, that were measured using ICP-AES. The samples consist of three different hydrothermal deposits; Jade chimney (Izena Cauldron), Hatoma chimney (Hatoma knoll) and Yoron chimney (Yoron hole), plus a manganese crust sample and seamount basalt and limestone substrates, where the latter three samples were obtained from the Takuyo #5 seamount. These were chosen as they are representative of the range of sediments and rock types found on the seamount and hydrothermal deposit on a back-arc setting in the NW Pacific.

Fig. 12A–F shows the spectra obtained from the samples, where all measurements were made in seawater using a single shot. A single 20 mJ pulse (energy at the target) of duration 250 ns was used, where all measurements were made with a gate delay and gate width of 500 ns. A spectrometer (Princeton Instruments SP2150) with a light throughput of f/4.0 and a 600 groove/mm grating was used to observe the emissions between 360 and 580 nm at 0.7 nm resolution using a 50 μm wide entrance slit, which is comparable to the specification of the spectrometer used

Table 3
Composition of sediment and rock samples obtained from the seafloor in the NW Pacific. Elements with concentrations > 1% are shown in bold.

Sample	Depth m	Zn %wt	Cu %	Pb %	Fe %	Mn %	Co %	Ni %	Mg %	Al %	Ca %	Ti %	Ag ppm	Sb ppm	As ppm
Jade chimney	1340	**19.80**	**4.39**	**12.20**	**10.20**	0.08	< 0.01	–	0.02	0.01	0.02	< 0.01	182	215	628
Hatoma chimney	1485	**12.00**	**5.25**	**10.30**	**3.50**	0.46	< 0.01	–	0.05	0.51	0.06	–	486	5940	7550
Yoron chimney	569	0.64	0.10	0.76	**2.52**	< 0.01	< 0.01	–	< 0.01	0.04	0.11	–	532	3330	8550
Manganese crust	1390	0.10	0.06	0.21	**9.50**	**16.20**	0.57	0.46	**1.03**	0.98	**6.32**	0.34	< 100	< 100	217
Basalt	1418	0.02	0.02	0.02	**8.66**	0.20	< 0.01	0.02	**4.99**	**6.79**	**9.96**	**1.45**	–	–	< 100
Limestone	1147	< 0.01	0.01	< 0.01	0.38	0.47	< 0.01	0.03	0.09	0.25	**25.20**	0.04	–	–	< 100

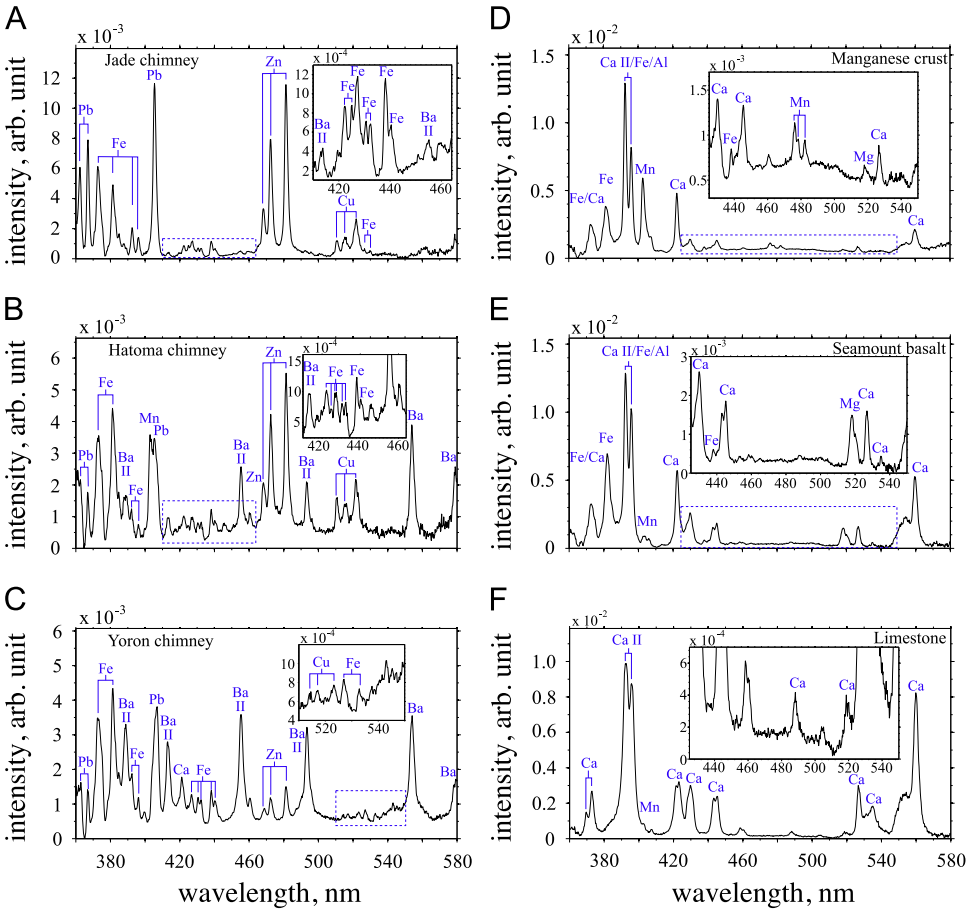

Fig. 12. Spectra of the (A) Jade chimney, (B) Hatoma chimney, (C) Yoron chimney hydrothermal deposits, (D) manganese crust and substrates of (E) seamount basalt and (F) limestone measured underwater using a single long-pulse. The metallic content of the samples are given in Table 3.

in ChemiCam. Powder pressed samples were used during the experiment to address the issue of sample in-homogeneity, so that the measurements are more representative of the whole rock composition shown in Table 3. The spectra have been normalized by the total integrated intensity across the observed wavelengths after subtraction of the background. All major metallic elements with concentrations > 1 wt% can be identified in the spectra with the exception of Ti and Al in the seamount basalt sample (with abundances of 1.45 and 6.79 wt%, respectively). With regards to Al, strong emissions at 394 and 396 nm (Kramida et al., 2013) are expected, but both wavelengths overlap with strong emissions of Ca (II) and Fe. While it is known that Ti emits a large number of peaks, these cannot be resolved from the background at the available wavelength resolution. On the other hand Zn, Pb, Cu can be identified in all three hydrothermal deposits (Fig. 12A–C), including the Yoron chimney sample (Fig. 12C), even though they are present in quantities < 1 wt%. The reason for the higher sensitivity for these elements is that they have strong emission lines at wavelengths that happen to be remote from the peaks of other elements in the matrix. The spectra of the Hatoma (Fig. 12B) and Yoron (Fig. 12C) chimney samples have characteristic peaks of Ba, which is known to be present in the form of barite ($BaSO_4$) in the deposits of low temperature vents. The maximum temperature of vent fluids when the Hatoma and Yoron chimneys were sampled were 280 and 247 °C, respectively, which is lower than the 320 °C vent fluids of the Jade chimney black smoker (Sakai et al., 1990). Due to the insolubility of barite, the concentration of Ba tends to be underestimated by ICP-AES analysis with the conventional acid digestion method used in this work, though it is noted that there was visible precipitation of needle-like barite crystals for these two samples and none of the others during preparation for ICP-AES measurement For the manganese crust sample, the major metallic elements, including Mg (1.03 wt%) can be identified. However, Co, Ni and Pb, which are present in similar

quantities to Zn, Pb, Cu in the Yoron chimney (<1 wt%) could not be identified. The major metallic elements in the seamount basalt and limestone samples can also be identified, with the exception of Al and Ti in the seamount basalt sample for the reasons mentioned earlier.

The relative abundances of Zn, Pb and Cu in the Jade and Hatoma chimney samples are determined from the LIBS measurements using the Boltzmann distribution law in Eq. (1). The condition in Eq. (3) has been modified as follows,

$$C'_s = \frac{N_s}{N_{Zn}+N_{Pb}+N_{Cu}}, \tag{5}$$

to give the relative abundance with respect to the total Zn, Pb and Cu content. Based on these values, we determine the Cu ratio (CR) and Zn ratio (ZR) as follows (Solomon, 1976),

$$CR = \frac{C'_{Cu}}{C'_{Cu}+C'_{Zn}} \times 100,$$
$$ZR = \frac{C'_{Zn}}{C'_{Zn}+C'_{Pb}} \times 100. \tag{6}$$

For the Jade chimney sample, the relative ratios determined for the underwater LIBS measurements are $CR_{LIBS}=16.7\pm6.4$ and $ZR_{LIBS}=64.6\pm8.6$, respectively, where the uncertainty is the standard deviation of 10 measurements. These compare favorably with the values of $CR_{ICP\text{-}AES}=18.1$ and $ZR_{ICP\text{-}AES}=61.9$ determined using ICP-AES. For the Hatoma chimney sample, the relative ratios are determined as $CR_{LIBS}=27.8\pm12.0$ and $ZR_{LIBS}=50.3\pm4.5$, respectively, which compare well with the actual values of $CR_{ICP\text{-}AES}=30.5$ and $ZR_{ICP\text{-}AES}=53.5$. The values are summarized in Table 4 and are also plotted in the ternary diagram in Fig. 13, along with the boundaries for mineral classification defined by Large (1992). Each dot in the figure corresponds to a single shot LIBS measurement and it can be seen that the LIBS measurements form clusters around the corresponding values determined from the ICP-AES analysis, shown as crosses in the figure. It should be noted that even though all three elements are detected in the Yoron sample (Zn=0.64, Pb=0.76, Cu=0.10 wt%), the same clustering technique was not effective due to the poor signal-to-noise ratio at these low concentrations.

Table 4
Relative abundance of Cu and Zn in the Jade and Hatoma chimney samples determined by LIBS and ICP-AES measurements, respectively.

Sample	CR_{LIBS}	$CR_{ICP\text{-}AES}$	ZR_{LIBS}	$ZR_{ICP\text{-}AES}$
Jade chimney	16.7 ± 6.4	18.1	64.6 ± 8.6	61.9
Hatoma chimney	27.8 ± 12.0	30.5	50.3 ± 4.5	53.5

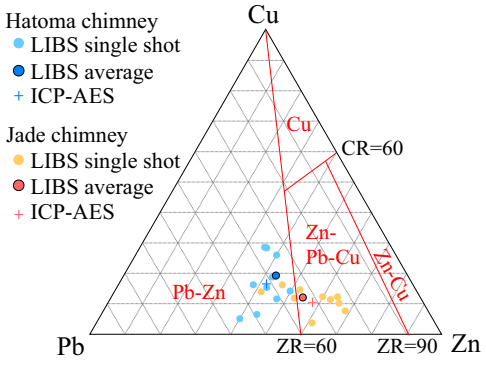

Fig. 13. Zn–Pb–Cu ternary diagram for underwater LIBS and ICP-AES measurements of the Jade and Hatoma chimneys.

4.3. Discussion of results and remaining challenges

The experiments and methods described demonstrate that information regarding the multi-element composition of bulk liquids and seawater immersed sediment and rock samples can be extracted from long-pulse LIBS measurements over concentration ranges that are relevant for oceanic applications. Although all the experiments were performed at atmospheric pressure, similar results can be expected at higher pressures since it has already been established that pressures up to 30 MPa do not have any significant effect on the quality of the signals obtained using a long-pulse for both liquids (Thornton et al., 2013) and immersed solids (Thornton et al., 2014a).

A novel method to quantify the concentrations of dissolved ions in bulk fluids has been developed that avoids the need for matrix-matched calibration curves. The method uses salinity as an external reference to compensate for matrix effect and can be used to generate a single set of calibration curves that can determine the concentration of Ca, Na, K and Li, with R^2 values of 0.9867, 0.9924, 0.9967 and 0.9973, respectively. A lower detection limit in the order of 25 μmol/kg has also been demonstrated for Li in seawater. For solids, detection limits in the order of 0.1 to 1.0 wt% have been demonstrated for Zn, Pb, Cu, Fe, Ca and Mn. Methods to characterize hydrothermal deposits have been developed based on CF-LIBS calculations using the total abundance of Zn, Pb and Cu as an internal standard. The relative abundance of Zn–Pb–Cu determined for seawater immersed mineral deposits show good agreement with the corresponding values calculated based on ICP-AES analysis.

The level of sensitivity demonstrated for solids is lower than for bulk liquids due to the significantly more complicated matrices and higher optical densities of the plasmas generated. It should be noted that non-metallic elements could not be detected over the range of wavelengths observed in our experiments, even though O, H and Cl are present in sufficient quantities in oceanic fluids for signals to be expected. Similarly, S, which constitutes a major component of the hydrothermal samples (sulfides and sulfates) and O, which constitutes a major component of manganese crusts (oxides), basalts (silicates) and limestones (carbonates), could not be detected in the immersed sediment and rock samples. Detection of these elements is commonly reported for measurements in a gaseous environment, where plasma temperatures of $>10{,}000$ K are typically achieved. Further studies are necessary to determine whether these elements and elements such as Si, C, Al and Ti can be observed underwater by extending the range of observed wavelengths.

Issues that have not yet been addressed with regard to on site measurements are the influence of temperature on the signals observed from vent fluids >200 °C and the influence of target in-homogeneity on measurements of mineral deposits. With regard to measurements at high temperatures, studies by Michel et al. (2007) demonstrated that elevated temperatures up to 100 °C have no observable affect on the spectral emissions. While further investigations are necessary to confirm this result for higher temperatures, measurement of high temperature vent fluids is expected to present a more practical problem when trying to focus the laser in fluids with strongly fluctuating temperatures and therefore refractive indices. Also measurements of fluids at these temperatures would require standoff measurements of at least a few tens of centimeters, which is not possible with our current system. For the present study, the applications are limited to the measurement of seawater and diffuse flows of temperatures <100 °C. With regard to in situ sediment and rock samples, target in-homogeneity is expected to have a strong influence on the signals obtained. In order to minimize the effects of target in-homogeneity, studies of rocks measured in a gaseous environment proposed performing multiple measurements (50 or more) of each target (Sallè et al., 2006; Clegg et al., 2009; Meslin et al., 2013;

Wiens et al., 2013). Since the spatial scales over which in-homogeneity occurs are dependent on the matrix, studies that specifically target seafloor sediments and rocks for a given laser spot size are necessary to evaluate the number of measurements required and also consider whether spatially scanned measurements are necessary to obtain data that is representative of whole rock composition.

5. Field deployment

ChemiCam was deployed using the ROV Hyper-Dolphin 3000 of the Japan Agency for Marine-Earth Science and Technology (JAMSTEC) at the Iheya North field in the Okinawa trough during November 2013 (see Fig. 8). Spectroscopic measurements of bulk liquids and mineral deposits were performed at depths of >1000 m. Fig. 14A shows the work class ROV about to be deployed with ChemiCam (fiber-optic setup) mounted in its central payload bay. The fiber-optic focusing unit can be seen held by the ROV right manipulator in Fig. 14B.

5.1. Survey area

The Iheya North field is a large, active hydrothermal vent area at a depth of 980 to 1040 m. Several artificial hydrothermal vents were drilled at this site during the International Ocean Discovery Program (IODP) 331 'Deep Hot Biosphere' expedition in October 2010 (Takai et al., 2010, 2012). Five of these drill holes have been preserved using steel casing pipes to enable post-drilling studies (Kawagucci et al., 2013). Measurements of seawater composition were performed using ChemiCam's direct optic setup, where salinity measurements were made using a SBE9plusCTD sensor (Seabird Co. Ltd.). Measurements of seawater composition were also performed near the C0016B artificial vent located $\sim$30 m from the North Big Chimney (NBC) mound, which was also drilled during the IODP 331 expedition. In addition, on site measurements using the fiber-optic setup were performed for solid test pieces and natural hydrothermal deposits that block the inside of the C0013E artificial hydrothermal vent. The C0013E vent, shown in Fig. 15A (Bodenmann et al., 2013), is a borehole drilled up to 54.5 m below seafloor (mbsf) during the IODP 331 expedition. The hole had been preserved using a steel casing pipe down to 40.2 mbsf and a triangular guide base at its opening enabled ROVs to access the vent opening. Vigorous discharge of hydrothermal fluids was observed from the vent's casing pipe up to 5 months after the hole was drilled, with temperatures of 309 °C (Kawagucci et al., 2013) recorded at the vent outlet. However, when observed half a year later, 11 months after drilling, the vent had become inactive, as hydrothermal deposits had blocked the opening of the steel casing pipe. Chimneys that had formed around the outside of the casing pipe were sampled at this time and were found to be anhydrite-rich ($CaSO_4$), with only minor components of Zn, Pb, Cu and Fe (Nozaki et al., 2013). However, the deposits blocking the inside of the casing pipe, seen in Fig. 15C, cannot be sampled because of their configuration.

5.2. Seawater measurements

Measurements of seawater composition were performed at depths of around 1000 m while the ROV cruised at 3–6 m altitude from the seafloor. The laser-pulse and observation conditions used during the sea trials were the same as those used in the experiments described in Section 4.1. Fig. 16 shows a typical spectrum of seawater measured during the ROV dive, where the signal shown is the average of 10 accumulated measurements that has been normalized by the total intensity after subtraction of the background. The corresponding salinity and depth measurements of the CTD sensor are written in the top right of the plot. The dotted line is the spectrum measured from a sample of seawater that was retrieved from the site, which was later measured at atmospheric pressure to allow for comparison. This sample was also measured using ICP-AES, with the results of the analysis summarized in Table 5. Fig. 17A shows the concentration of Na, Ca, K and Li determined from the LIBS signals, together with the salinity and depth measurements of the CTD (Fig. 17B) measured as the ROV travelled along a 100 m long transect, passing over the NBC chimney and the C0016B artificial vent.

The major metallic ions in seawater, Na, Ca, K, Mg, as well as Li are clearly visible in the in situ measurements. The concentrations of Na, K, Ca in Fig. 17A remain essentially the same along the transect, with average and standard deviations of 470 ± 2, 10.3 ± 0.2 and 9.7 ± 1.0 mmol/kg, respectively. These values are in good agreement with typical values for seawater (see Table 2) and agree within 5% of the concentrations of the seawater sample retrieved from this area, which had concentrations of 452, 10.2 and 9.4 mmol/kg, respectively (see Table 5). The standard deviation for Ca is relatively large due to the poor sensitivity of the optical setup used for wavelengths <480 nm. The average concentration of Li along the transect is 25 ± 9 μmol/kg, where the relatively large standard deviation is due to the fact that the Li peak itself is small and so the effects of statistical uncertainty are large. An increase in Li concentration is seen as the ROV passes over the C0016B artificial vent, which may be due to the influence of the vent fluids. However, no changes in salinity or in the concentrations of the other major ions were seen in the data at this point. While the average concentration

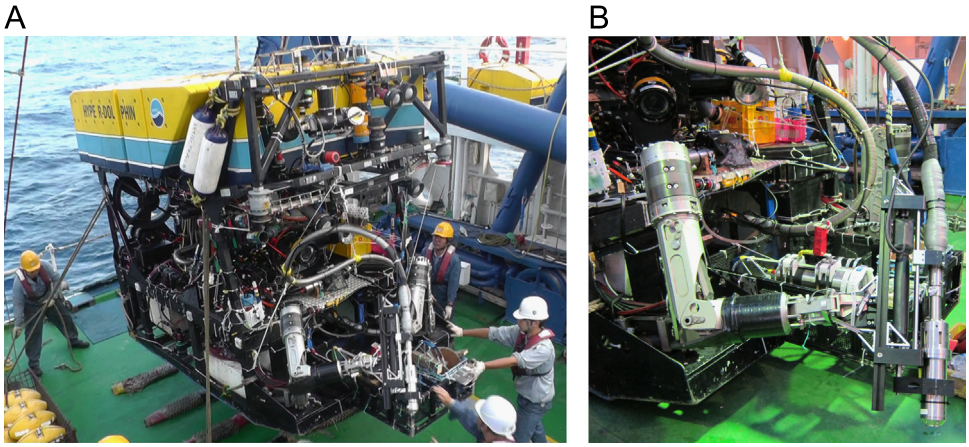

Fig. 14. (A) ChemiCam mounted on the ROV Hyper-Dolphin 3000 about to be deployed in the Okinawa trough, and (B) a close-up of the linearly actuated focusing probe held by the ROV's manipulator.

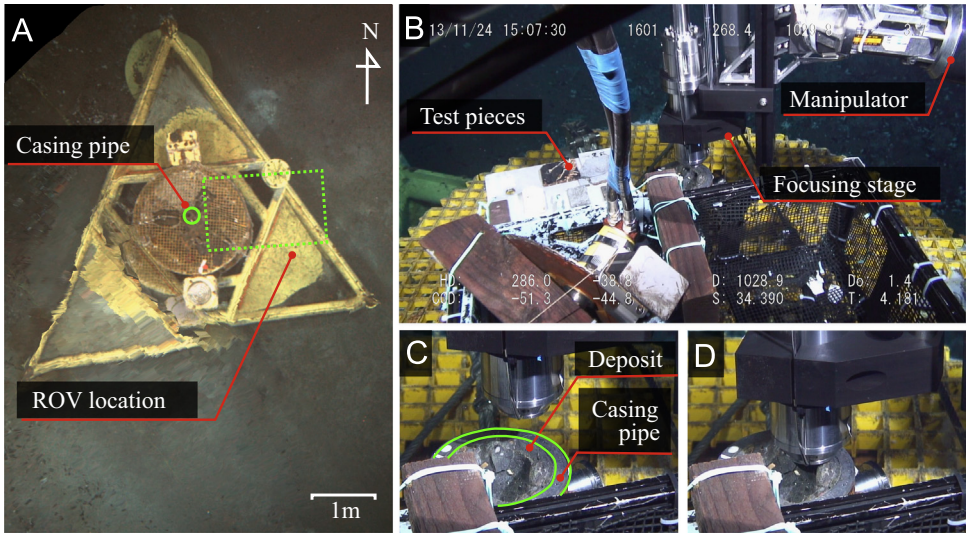

Fig. 15. (A) A top view of the C0013E measured using the seaXerocks mapping system (Bodenmann et al., 2013). The depth of the seafloor is 1034 m in this area. (B) Shows the ROV manipulator holding ChemiCam's focusing probe (C) shows the deposits that currently block the vent and (D) shows measurements of the deposits being performed.

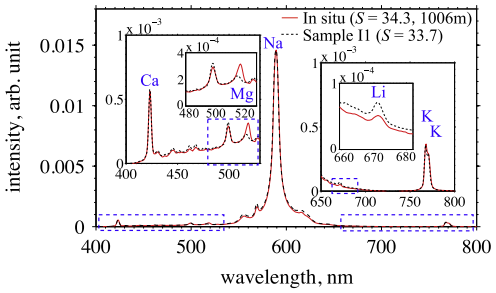

Fig. 16. Typical spectrum measured in situ at the Iheya North field at a depth of 1006 m, shown in red, compared to the spectrum of a sample retrieved from where the in situ measurements were performed, which is shown as a dotted line. The measurements of the sample were performed at atmospheric pressure. Both spectra are the average of 10 measurements. (For interpretation of the references to color in this figure legend, the reader is referred to the web version of this article.)

Table 5
Comparison of in situ LIBS measurements of seawater composition and ICP-AES analysis of seawater sampled in the vicinity.

Description	Na mmol/kg	K mmol/kg	Ca mmol/kg	Li μmol/kg
In situ	470 ± 2	10.3 ± 0.2	9.7 ± 1.0	25 ± 9
Sample I1 (ICP-AES)	452	10.2	9.4	43.2

of Li along the transect agrees well with the values typical for seawater, the value is about 40% smaller than the Li concentration of the sample retrieved from this area, which was obtained when the ROV passed over the NBC chimney. The high concentration of Li in the sample is also seen in the spectrum shown as a dotted line in Fig. 16, where the Li peak at 670.8 nm is noticeably larger than for the typical in situ measurements. It is noted however, that while there are some small fluctuations in salinity occurring as the ROV passes over the NBC chimney, no changes in chemical composition are seen in the LIBS measurements.

The measurements made in situ do not show any noticeable effect from hydrothermal fluids other than Li near the C0016B vent and some small fluctuations in salinity measured by the CT sensor. The reason for this is because the measurements were made at an altitude of a few meters, at which point the hydrothermal fluids from the NBC chimney and C0016B are mixed and diluted by

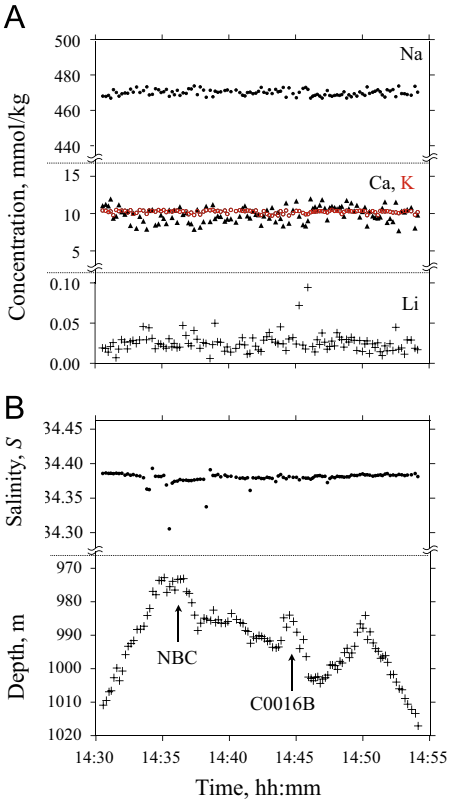

Fig. 17. (A) Multi-element time series from in situ LIBS measurements and corresponding (B) salinity and depth measurements.

the surrounding seawater. Another point is that the analysis is performed on the average of 10 accumulated measurements and it is possible that small local changes are averaged out during the 10 s period over which the signal is accumulated.

5.3. Measurement of hydrothermal deposits

Metallic alloys and rock test pieces, visible in Fig. 15B, were mounted on the basket of the ROV and measurements were made at various depths between 0 and 1000 m during the ROV's descent to

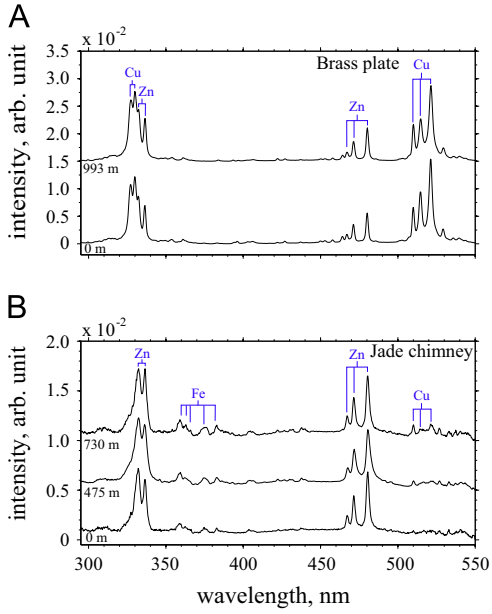

Fig. 18. Measurements of sample test pieces during sea trials with the ROV. (A) shows single shot spectra of a brass alloy measured near the sea-surface, and at a depth of 993 m. (B) shows single shot measurements of the Jade chimney sample, measured near the sea-surface, and at depths of 475, and 730 m, respectively. Measurements made at different depths have been offset vertically for better visualization.

the seafloor. The main objective of the measurements was to verify that the fiber-optic focusing probe could be focused onto a target's surface using the ROV manipulator. The ROV operators were able to bring the probe near to the test pieces, which had dimensions of 5×3 cm, without difficulty and the linear stage was used to focus the laser onto each target. The process took between 1 and 2 min for each sample, after which multiple measurements could be made. Fig. 18 shows the spectra measured from (A) a brass plate and (B) the Jade chimney sample, where all measurements were made using a single 20 mJ pulse of duration 250 ns with an observation gate delay of 800 ns and gate width of 500 ns. The spectra have been normalized by the total integrated intensity across the observed wavelengths after subtraction of the background. The bottom most spectra are for measurements made near the sea-surface and measurements made at different depths, noted at the bottom left of each spectrum, have been offset vertically for better visualization. The effects of pressure are not seen in the data. Some shot to shot variations are seen for the Jade chimney measurements, where although the peaks of Zn and Fe are detected in all the measurements, the peaks of Cu are only detected in some of the spectra obtained. It should be noted that the prominent signal of Pb at 405 nm in Fig. 12A, is not seen in any of the spectra obtained from the Jade chimney chip that was used as a test piece. The difference between the spectra obtained in the laboratory and those obtained during the sea trials is thought to be due to sample in-homogeneity, since rock chips were used during the experiments at sea. Rock chips were chosen since they are physically robust and we were concerned that the forces during deployment and recovery of the ROV may destroy the more fragile pressed pellets. Even though the Jade chimney rock chip was extracted from the same sample used to make the pellets, it is possible that the part of the sample used for the chip consisted mainly of sphalerite or wurtzite ((Zn,Fe)S) with some chalcopyrite ($CuFeS_2$) and pyrite (FeS_2) fractions but contained hardly any galena (PbS).

Fig. 19 shows an example of a single-shot spectrum measured in situ, at a depth of 1032 m, of deposits inside the steel casing pipe of the C0013E vent. Though not all the emission lines have been identified, well-resolved lines of Zn, Pb, Cu and Fe can be seen. The relative abundance determined from the LIBS signal of Zn, Pb and

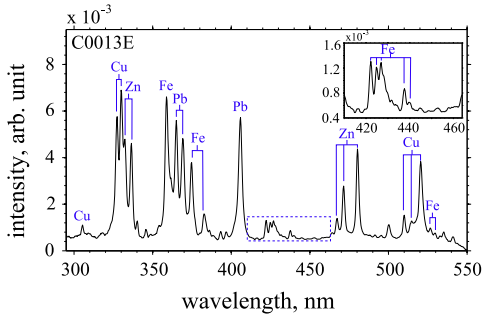

Fig. 19. Single shot measurement of the hydrothermal deposits in the C0013E casing pipe. The deposits, visible in Fig. 15C and D were measured in situ at a depth of 1032 m. Well-resolved lines of Zn, Pb, Cu, and Fe can be seen in the spectrum.

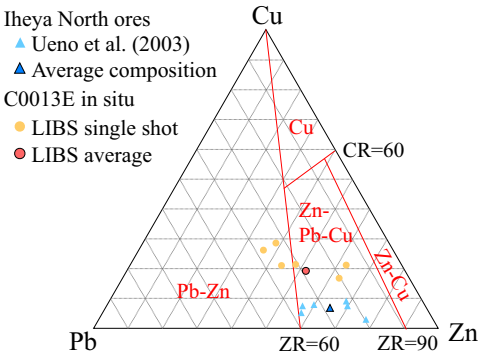

Fig. 20. Zn–Pb–Cu ternary diagram of the in situ measurements of the deposits in the C0013E vent determined from the LIBS measurements in comparison to typical Iheya North field ores analyzed by Ueno et al. (2003).

Cu in the deposits are plotted in the ternary diagram in Fig. 20. The values of CR_{C0013E} and ZR_{C0013E} are 32.1 ± 8.7 and 62.3 ± 12.5, respectively, indicating that the deposit is a Zn–Pb–Cu type, or kuroko-ore according to the classification of Large (1992). Ca was not detected in any of the measurements made, indicating that the composition of the deposits inside the vent orifice are different to those sampled from the outside of the pipe 11 months after it was installed, 2 years prior to the measurements in this work, which were reported to be anhydrite rich (Nozaki et al., 2013). Due to their configuration, sampling of the deposits was not possible and so we can only compare the results to values typical for the area, which are described by Ueno et al. (2003). Hydrothermal deposits sampled between 1996 and 1998, i.e. before the artificial vents were installed, from the NBC chimney, located 100 m from where the C0013E vent is now located, have values of $CR_{Iheya} = 8.9 \pm 3.1$ and $ZR_{Iheya} = 69.7 \pm 8.3$, respectively. This indicates that, while the relative abundance of zinc in the deposits blocking the C0013E vent are comparable to the values typical for the area, with $ZR_{C0013E}/ZR_{Iheya} = 0.9 \pm 0.2$, the relative abundance of copper is significantly higher than the typical value, with $CR_{C0013E}/CR_{Iheya} = 3.6 \pm 0.4$, where the values are summarized in Table 6.

The relatively high Cu content of deposits in the vent orifice is attributed to the fact that $CuFeS_2$ precipitates at higher temperatures than (Zn,Fe)S, which in turn precipitates at higher temperatures than PbS (Halbach et al., 1993; Hannington et al., 1995). Typically, hydrothermal fluids mix with seawater underground before reaching the seafloor as they pass through porous layers of rock. In this case, precipitation starts to occur underground and since $CuFeS_2$ precipitates early on in the mixing phase, i.e. at higher temperatures, it tends to be deposited deeper beneath the seafloor than (Zn,Fe)S and PbS. This produces the sequence from bottom to top of quartz-chalcopyrite-rich siliceous ore (keiko-ore), chalcopyrite-pyrite-rich yellow ore (oko-ore), sphalerite-galena-rich black ore (kuroko-ore)

Table 6
Relative abundance of Cu and Zn determined from in situ measurements of deposits blocking the casing pipe of the C0013E vent, compared to typical values for the Iheya North field as given in Ueno et al. (2003).

Description	CR	ZR
C0013E in situ	32.1 ± 8.7	62.3 ± 12.5
Iheya North (Ueno et al., 2003)	8.9 ± 3.1	69.7 ± 8.3
C0013E/Iheya North	3.6 ± 0.4	0.9 ± 0.2

and quartz-hematite-rich sedimentary rock, which is the sequence typically observed in volcanogenic massive sulfide deposits on land (Ohmoto, 1996). Considering that land-based volcanogenic massive sulfide deposits are ancient counterparts of modern seafloor hydrothermal deposit in a back-arc setting, it follows that most exposed deposits on the seafloor, such as those analyzed in Ueno et al. (2003), would be formed by precipitation of hydrothermal fluids that have been partially depleted of Cu. This is consistent with the fact that the chimney samples analyzed in Ueno et al. (2003) contain barite, which is known to precipitate at lower temperatures than chalcopyrite (Hannington et al., 1995). In the case of the deposits inside the C0013E casing pipe, hydrothermal fluids enter the pipe at a depth of 40.2 mbsf. The hot fluids remain isolated as they rise up the pipe and maintain a high temperature until they mix with seawater at the vent orifice a few meters above the seafloor. In this situation, the pure, undepleted vent fluids are rapidly quenched through sudden exposure to seawater at the vent outlet and the precipitates formed include high temperature mineral fractions, such as $CuFeS_2$, that would normally precipitate deeper underground, or in the central part of chimney structures. The high CR ratio of the deposits blocking the C0013E casing pipe are a result of the fact that they are formed from undepleted vent fluids and as such, it can be considered that their composition is representative of the end member for relative Cu abundance at this site.

6. Conclusion and future

We have developed and successfully deployed a deep-sea LIBS instrument to study the chemical composition of seawater and mineral deposits at depths of more than 1000 m. The instrument can be deployed from a ROV and has the unique ability to perform in situ, multi-element analysis of both liquids and solid deposits at depths of up to 3000 m. Practical challenges associated with the operation of the device have been overcome and laboratory quality spectra were successfully measured during sea trials in an active hydrothermal vent field. While this paper describes deployment from a ROV, the electrical interface required to operate the instrument is standard on most scientific platforms and the instrument could just as easily be deployed from a human operated vehicle (HOV) that is equipped with a manipulator. While measurement of solids rely on the skill of human operators, the measurement of fluids do not require any focusing or manipulator operation and can be performed from an autonomous underwater vehicle (AUV) or fixed platform, as long as sufficient power and, in the case of an AUV, sufficient buoyancy can provided.

With regard to the measurements of liquids, sufficient sensitivity has been demonstrated to detect the major elements (Na, Mg, Ca, K) and Li over the range of concentrations that is relevant for oceanic applications. A method to quantify the concentration of dissolved ions has been developed that allows for simultaneous multi-element studies of Na, Ca, K and Li using just a single set of calibration-curves, where the lowest level of detection achieved in this work is 25 μmol/kg for Li in seawater. With regard to measurements of mineral deposits, reliable detection of elements with concentrations > 1.0 wt% can be achieved and we demonstrate that underwater long-pulse LIBS measurements are effective for discriminating between different types of hydrothermal deposit, manganese crusts, seamount basalt and limestone. Methods to determine the relative abundance of Zn, Pb and Cu in hydrothermal deposits have been developed and show good agreement with the results of ICP-AES measurements. While detection of elements with lower concentrations, ~ 0.1 wt%, are also demonstrated, the detected peaks are not suitable for analysis due to the poor signal-to-noise ratio. During sea trials in the Iheya North field, in situ multi-element analysis of seawater and mineral deposits was achieved for the first time in the deep-sea environment. Measurements of seawater composition at 1000 m depth showed good agreement with the results of sampling, verifying the practical application of the instrument and data processing methods developed in this work. In situ measurements of mineral deposits blocking an artificial hydrothermal vent at a depth of more than 1000 m indicated that while the ratio of Zn to Pb remains comparable to hydrothermal deposits in this region, the abundance of Cu relative to Zn in these deposits is more than $3\times$ the typical ratio for deposits in this area.

Our future work will focus on increasing the operational efficiency of the instrument for measurement of seafloor sediments and rocks. We plan on developing an auto-focus system with tracking capabilities to enable scanned measurement of rough surfaces. We also plan to look into the use of a deep-sea grinder or rotary blade to enable sub-surface measurements, since weathering of exposed surfaces may favor certain elements and result in a bias. The application of signal processing techniques such as multivariate analysis and database matching techniques will also be investigated with the aim of quantifying the measurements of solid deposits. It is hoped that through integration with platforms such as underwater vehicles, drilling systems and subsea observatories, this technology can enable higher resolution geochemical studies of the seafloor and enable informed decisions to be made based on the real-time measurements of the device.

Acknowledgements

The authors would like to thank the Hyper-Dolphin 3000 team and R/V Natsushima crew for their assistance during the NT13-23 cruise. They would also like to thank T. Fujii, T. Urabe, A Usui, T. Fukuba, K. Okamura, T. Noguchi, K. Suzuki, T. Masamura, M. Sasano and Y. Nakajima for their support collecting and analyzing samples and their help during experiments with ChemiCam. We thank members of the steering panel; T. Takeuchi, T. Fujii, K. Iizasa, the late K. Tamaki, T. Ura, H. Sugimatsu, T. Yamamoto, K. Okino and J. Ishibashi for the stimulating discussions and advice given during the various stages of this project.

The project is funded by the Japanese Ministry of Education under the 'Program for the development of fundamental tools for the utilization of marine resources'.

References

Aguilera, J.A., Arago, C., 2007. Multi-element Saha-Boltzmann and Boltzmann plots in laser-induced plasmas. Spectrochim. Acta Part B 62, 378–385.

Arca, G., Ciucci, A., Palleschi, V., Rastelli, S., Tognoni, E., 1997. Trace element analysis in water by the laser-induced break-down spectroscopy technique. Appl. Spectrosc. 51, 1102–1105.

Bodenmann, A., Thornton, B., Nakajima, R., Yamamoto, H., Ura, T., 2013. Wide area 3D seafloor reconstruction and its application to sea fauna density mapping. In: Proceedings of MTS/IEEE Oceans '13, San Diego, 130504-006.

Brewer, P.G., Malbya, G., Pasteris, J.D., White, S.N., Peltzer, E.T., Wopenka, B., Freeman, J., Brown, M.O., 2004. Development of a laser Raman spectrometer for deep-ocean science. Deep-Sea Res. I 51, 739–753.

Ciucci, A. Corsi, Palleschi, M., Rastelli, V., Salvetti, S., Tognoni, E., A., 1999. New procedure for quantitative elemental analysis by laser-induced plasma spectroscopy. Appl. Spectrosc. 53, 960–964.

Clegg, S.M., Sklute, E., Dyar, M.D., Barefield, J.E., Wiens, R.C., 2009. Multivariate analysis of remote laser-induced breakdown spectroscopy spectra using partial least squares, principal component analysis, and related techniques. Spectrochim. Acta Part B 64, 79–88.
Colao, F., Fantoni, R., Lazic, V., Caneve, L., Giardini, A., Spizzichino, V., 2004. LIBS as a diagnostic tool during the laser cleaning of copper based alloys: experimental results. J. Anal. At. Spectrom. 19, 502–504.
Cremers, D.A., Radziemski, L.J., Loree, T.R., 1984. Spectrochemical analysis of liquids using the laser spark. Appl Spectrosc. 38, 721–729.
De Giacomo, A., Dell'Aglio, M., Colao, F., Fantoni, R., Lazic, V., 2005. Double-pulse LIBS in water bulk and on submerged bronze samples. Appl. Surf. Sci. 247, 157–162.
De Giacomo, A., Dell'aglio, M., De Pascale, O., Longo, S., Capitelli, M., 2007. Laser induced breakdown spectroscopy on meteorites. Spectrochim. Acta Part B 62, 1606–1611.
De Giacomo, A., De Bonis, A., Dell'Aglio, M., De Pascale, O., Gaudiuso, R., Orlando, S., Santagata, A., Senesi, G.S., Taccogna, F., Teghil, R., 2011. Laser ablation of graphite in water in a range of pressure from 1 to 146 atm using single and double pulse techniques for the production of carbon nanostructures. J. Phys. Chem. C 115, 5123–5130.
Eppler, A.S., Cremers, D.A., Hickmott, D.D., Ferris, M.J., Koskelo, A.C., 1996. Matrix effects in the detection of Pb and Ba in soils using laser-induced breakdown spectroscopy. Appl. Spectrosc. 51, 1175–1181.
Fichet, P., Mauchien, P., Wagner, J.F., Moulin, C., 2001. Quantitative elemental determination in water and oil by laser induced breakdown spectroscopy. Anal. Chim. Acta 429, 269–278.
Fichet, P., Menut, D., Brennetot, R., Vors, E., Rivoallan, A., 2003. Analysis by laser-induced breakdown spectroscopy of complex solids, liquids, and powders with an echelle spectrometer. Appl. Opt. 42, 6029–6039.
Fukuba, T., Provin, C., Okamura, K., Fujii, T., 2009. Development and evaluation of microfluidic device for Mn ion quantification in ocean environments. IEEJ Trans. Sens. Micromach. 129, 69–72.
Halbach, P., Pracejus, B., Märten, A., 1993. Geology and mineralogy of massive sulfide ores from the Central Okinawa Trough, Japan. Econ. Geol. 88, 2210–2225.
Hannington, M.D., Jonasson, I.R., Herzig, P.M., Petersen, S., 1995. Physical and chemical processes of seafloor mineralization at mid-ocean ridges In:. In: Humphris, S.E., Zierenberg, R.A., Mullineaux, L.S., Thomson, R.E. (Eds.), Seafloor Hydrothermal Systems: Physical, Chemical, Biological, and Geological Interactions. Geophysical Monograph Series, 91. American Geophysical Union, Washington, DC, pp. 115–157.
Harmon, R.S., De Lucia, F.C., Miziolek, A.W., McNesby, K.L., Walters, R.A., French, P.D., 2005. Laser-induced breakdown spectroscopy (LIBS)—an emerging field-portable sensor technology for real-time, in-situ geochemical and environmental analysis. Geochem. Explor Environ. Anal. 5, 21–28.
Herrera, K., Tognoni, E., Omenetto, N., Gornushkin, I.B., Smith, B.W., Winefordner, J. D., 2009a. Comparative study of two standard-free approaches in laser-induced breakdown spectroscopy as applied to the quantitative analysis of aluminum alloy standards under vacuum conditions. J. Anal. At. Spectrom. 24, 426–438.
Herrera, K., Tognoni, E., Smith, B.W., Omenetto, N., Winefordner, J.D., 2009b. Semi-quantitative analysis of metal alloys, brass and soil samples by calibration-free laser-induced breakdown spectroscopy: recent results and considerations. J. Anal. At. Spectrom. 24, 413–425.
Hou, H., Tian, Y., Li, Y., Zheng, R., 2014. Study of pressure effects on laser induced plasma in bulk seawater. J. Anal. At. Spectrom. 29, 169–175.
Huang, J.S., Ke, C.B., Lin, K.C., 2004. Matrix effect on emission current correlated analysis in laser-induced breakdown spectroscopy of liquid droplets. Spectrochim. Acta Part B 59, 321–326.
Hunter, A.J.R., Piper, L.G., 2006. Spark-induced breakdown spectroscopy: a description of an electrically generated LIBS-like process for elemental analysis of airborne particulates and solid samples. In: Miziolek, A.W., Palleschi, V., Schechter, I. (Eds.), Laser Induced Breakdown Spectroscopy. Cambridge University Press, pp. 585–614.
Ishibashi, J., Noguchi, T., Toki, T., Miyabe, S., Yamagami, S., Ohnishi, Y., Yamanaka, T., Yokoyama, Y., Omori, E., Takahashi, Y., Hatada, K., Nakaguchi, Y., Yoshizaki, M., Konno, U., Shibuya, T., Takai, K., Unagaki, F., Kawagucchi, S., 2014. Diversity of fluid geochemistry affected by processes during fluid upwelling in active hydrothermal fields in the Izena Hole, the middle Okinawa Trough back-arc basin. Geochem. J. 48, 1–13.
Kawagucci, S., Chiba, H., Ishibashi, J., Yamanaka, T., Toki, T., Muramatsu, Y., Ueno, Y., Makabe, A., Inoue, K., Yoshida, N., Nakagawa, S., Nunoura, T., Takai, K., Takahata, N., Sano, Y., Narita, T., Teranishi, G., Obata, H., Gamo, T., 2011. Hydrothermal fluid geochemistry at the Iheya North field in the mid-Okinawa Trough: implication for origin of methane in subseafloor fluid circulation systems. Geochem. J. 45, 109–124.
Kawagucci, S., Miyazaki, J., Nakajima, R., Nozaki, T., Takaya, Y., Kato, Y., Shibuya, T., Konno, U., Nakaguchi, Y., Hatada, K., Hirayama, H., Fujikura, K., Furushima, Y., Yamamoto, H., Watsuji, T., Ishibashi, J., Takai, K., 2013. Post-drilling changes in fluid discharge pattern, mineral deposition, and fluid chemistry in the Iheya North hydrothermal field, Okinawa Trough. Geochem. Geophys. Geosyst. 14, 4774–4790.
Kennedy, P.K., Boppart, S.A., Hammer, D.X., Rockwell, B.A., Noojin, G.D., Roach, W.P., 1995. A first-order model for computation of laser-induced breakdown thresholds in ocular and aqueous media: Part II—Comparison to experiment. IEEE J. Quantum Electron. 31, 2250–2257.
Kennedy, P.K., Hammer, D.X., Rockwell, B.A., 1997. Laser-induced breakdown in aqueous media. Prog. Quantum Electron. 21, 155–248.
Kennish, M.J., 2000. Practical Handbook of Marine Science, third ed. CRC Press p. 896.
Kirk, J.T.O., 1983. Light and Photosynthesis is Aquatic Ecosystems, second ed. Cambridge University Press, Cambridge p. 509.
Kirk, J.T.O., 1994. Estimation of the absorption and the scattering coefficients of natural waters by use of underwater irradiance measurements. Appl. Opt. 33, 3267–3278.
Kramida A., Ralchenko. Yu., Reader, J. NIST ASD Team, 2013. NIST Atomic Spectra Database version 5.1. [Online Available: ⟨http://physics.nist.gov/asd⟩ [Monday, 28-Jul-2014 11:26:56 EDT]. National Institute of Standards and Technology, Gaithersburg, MD.
Large, R.R., 1992. Australian volcanic-hosted massive sulphide deposits: features, styles and genetic models. Econ. Geol. 87, 471–510.
Lawrence-Snyder, M., Scaffidi, J., Angel, S.M., Michel, A.P.M., Chave, A.D., 2007. Sequential-pulse laser-induced breakdown spectroscopy of high-pressure bulk aqueous solutions. Appl. Spectrosc. 61, 171–176.
Lazic, V., Colao, F., Fantoni, R., Spizzicchino, V., 2005. Recognition of archeological materials underwater by laser induced breakdown spectroscopy. Spectrochim. Acta Part B 60, 1014–1024.
Lazic, V., Colao, F., Fantoni, R., Spizzicchino, V., Jovićević, S., 2007. Underwater sediment analyses by laser induced breakdown spectroscopy and calibration procedure for fluctuating plasma parameters. Spectrochim. Acta Part B 62, 30–39.
Lo, K., Cheung, N., 2002. ArF laser-induced plasma spectroscopy for part-per-billion analysis of metal ions in aqueous solutions. Appl. Spectrosc. 56, 682–688.
Luther III, G.W., Rozan, T.F., Taillefert, M., Nuzzio, D.B., Di Meo, C., Shank, T.M., Lutz, R.A., Cary, S.C., 2001. Chemical speciation drives hydrothermal vent ecology. Nature 410, 813–816.
Malitson, I.H., 1965. Interspecimen comparison of the refractive index of fused silica. J. Opt. Soc. Am. 55, 1205–1208.
Masamura, T., Thornton, B., Ura, T., 2011. Spectroscopy and imaging of laser-induced plasmas for chemical analysis of bulk aqueous solutions at high pressures. In: Proceedings of MTS/IEEE Oceans '11 Kona, 110423-002.
Maurice, S., Wiens, R.C., Saccoccio, M., Barraclough, B., Gasnault, O., et al., 2012. The ChemCam instrument suite on the Mars Science Laboratory (MSL) rover: science objectives and mast unit description. Space Sci. Rev. 170, 95–166.
Meslin, P.Y., Gasnault, O., Forni, O., Schröder, S., Cousin, A., 55 more authors and the MSL Science Team, 2013. Soil diversity and hydration as observed by ChemCam at Gale Crater, Mars. Science 341, 1238670.
Michel, A.P.M., Lawrence-Snyder, M., Angel, S., Chave, A., 2007. Laser-induced breakdown spectroscopy of bulk aqueous solutions at oceanic pressures: evaluation of key measurement parameters. Appl. Opt. 46, 2507–2515.
Michel, A.P.M., Chave, A., 2008a. Single pulse laser-induced breakdown spectroscopy of bulk aqueous solutions at oceanic pressures: interrelationship of gate delay and pulse energy. Appl. Opt. 47, 131–143.
Michel, A.P.M., Chave, A., 2008b. Double pulse laser-induced breakdown spectroscopy of bulk aqueous solutions at oceanic pressures: interrelationship of gate delay and pulse energies, interpulse delay, and pressure. Appl. Opt. 47, 123–130.
Miziolek, A.W., Palleschi, V., Schechter, I., 2006. Laser-induced Breakdown Spectroscopy. Cambridge University Press p. 640.
Morel, A., 1974. Optical properties of pure water and pure seawater. In: Jerlov, N.G., Nielsen, E.S. (Eds.), Optical Aspects of Oceanography. Academic Press, New York, pp. 1–24.
Mosier-Boss, P.A., Lieberman, S.H., Theriault, G.A., 2002. Field demonstrations of a direct Push FO-LIBS metal sensor. Environ. Sci. Technol. 36, 3968–3976.
Nozaki, T., Ishibashi, J., Shimada, K., Takaya, Y., Kato, Y., Kawagucci, S., Shibuya, T., Takai, K., 2013. Geochemical signature of the zero-age chimney formed on artificial hydrothermal vents created by IODP Exp. 331 in the Iheya North field, Okinawa Trough. In: Proceedings of the 12th SGA Biennial Meeting 2, 561–561.
Nuzzio, D.B., Taillefert, M., Cary, S.C., Reysenbach, A.L., Luther III, G.W., 2002. In situ voltammetry at deep-sea hydrothermal vents. Environ. Electrochem., 40–51.
Nyga, R., Neu, W., 1993. Double-pulse technique for optical emission spectroscopy of ablation plasmas of samples in liquids. Opt. Lett. 18, 747–749.
Ohmoto, H., 1996. Formation of volcanogenic massive sulfide deposits: the Kuroko perspective. Ore Geol. Rev. 10, 135–177.
Okamura, K., Kimoto, H., Saeki, K., Ishibashi, J., Obata, H., Maruo, M., Gamo, T., Nakayama, E., Nozaki, Y., 2001. Development of a deep-sea in situ Mn analyzer and its application for hydrothermal plume observation. Mar. Chem. 76, 17–26.
Perkin, R.G., Lewis, E.L., 1980. The practical salinity scale 1978: fitting the data. J. Oceanic Eng. 5, 9–16.
Pichahchy, A.E., Cremers, D.A., Ferris, M.J., 1997. Elemental analysis of metals under water using laser-induced breakdown spectroscopy. Spectrochim. Acta Part B 52, 25–39.
Praher, B., Palleschi, V., Viskup, Heitz, J., Pedarnig, J.D., 2010. Calibration free laser-induced breakdown spectroscopy of oxide materials. Spectrochim. Acta Part B 65, 671–679.
Prieur, L., Sathyendranath, S., 1981. An optical classification of coastal and oceanic waters based on the specific spectral absorption curves of phytoplankton pigmens, dissolved organic matter and other particulate materials. Limnol. Oceanogr. 26, 671–689.
Provin, C., Fukuba, T., Okamura, K., Fujii, T., 2013. An integrated microfluidic system for manganese anomaly detection based on chemiluminescence: description and practical use to discover hydrothermal plumes near the Okinawa Trough. IEEE J. Ocean Eng. 38, 178–185.

Saeki, M., Iwanade, A., Ito, C., Wakaida, I., Thornton, B., Sakka, T., Ohba, H., 2014. Development of a fiber-coupled laser-induced breakdown spectroscopy instrument for analysis of underwater debris in a nuclear reactor core. J. Nucl. Sci. Technol. 51, 930–938.

Sakai, H., Gamo, T., Kim, E.S., Tsutsumi, M., Tanaka, T., Ishibashi, J., Wakita, H., Yamano, M., Oomori, T., 1990. Venting of carbon dioxide-rich fluid and hydrate formation in mid-okinawa trough backarc basin. Science 248, 1093–1096.

Sakka, T., Takatani, K., Ogata, Y.H., Mabuchi, M., 2002. Laser ablation at the solid–liquid interface: transient absorption of continuous spectral emission by ablated aluminium atoms. J. Phys. D Appl. Phys. 35, 65–73.

Sakka, T., Oguchi, H., Masai, S., Hirata, K., Ogata, Y.H., Saeki, M., Ohba, H., 2006. Use of a long-duration ns pulse for efficient emission of spectral lines. Appl. Phys. Lett. 88, 061120.

Sakka, T., Yamagata, H., Oguchi, H., Fukami, K., Ogata, Y.H., 2009. Emission spectroscopy of laser ablation plume: composition analysis of a target in water. Appl. Surf. Sci. 255, 9576–9580.

Sakka, T., Tamura, A., Matsumoto, A., Fukami, K., Nishi, N., Thornton, B., 2014. Effects of pulse width on nascent laser-induced bubbles for underwater laser-induced breakdown spectroscopy. Spectrochim. Acta Part B 97, 94–98.

Sallè, B., Lacour, J.L., Mauchien, P., Fichet, P., Maurice, S., Manhès, G., 2006. Comparative study of different methodologies for quantitative rock analysis by laser-induced breakdown spectroscopy in a simulated Martian atmosphere. Spectrochim. Acta Part B 61, 301–313.

Samek, O., Beddows, D., Kaiser, J., Kukhlevsky, S., Liska, M., Telle, H., Young, J., 2000. Application of laser-induced breakdown spectroscopy to in situ analysis of liquid samples. Opt. Eng. 39, 2248–2262.

Smith, P.L., Heise, C., Esmond, J.R., Kurucz, R.L., 2014. Atomic Line Database. Available: ⟨http://www.cfa.harvard.edu/amdata/ampdata/kurucz23/sekur.html⟩ [2014, March 15].

Solomon, M., 1976. Volcanic massive sulphide deposits and their host rocks—a review and an explanation. In: Wolf, K.A. (Ed.), Handbook of Strata-bound and Stratiform Ore Deposits II, Regional Studies and Specific Deposits: Amsterdam. Elsevier, pp. 21–50.

St-Onge, L., Kwong, E., Sabsabi, M., Vadas, E., 2004. Rapid analysis of liquid formulations containing sodium chloride using laser-induced breakdown spectroscopy. J. Pharmaceut. Biomed. Anal. 36, 277–284.

Takahashi, T., Thornton, B., Ura, T., 2013. Investigation of influence of hydrostatic pressure on double-pulse laser-induced breakdown spectroscopy for detection of Cu and Zn in submerged solids. Appl. Phys. Express 6, 042403.

Takahashi, T., Thornton, B., Sato, T., Ohki, K., Sakka, T., 2014. Quantitative chemical analysis of submerged solids using calibration-free laser-induced breakdown spectroscopy. In: Proceedings of MTS/IEEE Oceans '14, St. John's, NL, 140326-120.

Takai, K., Mottl, M.J., Nielsen, S.H.H., IODP Expedition 331 Scientists, 2010. Deep hot biosphere IODP Expedition 331 Preliminery Report. Integrated Ocean Drilling Program Management International Incorporated, 63.

Takai, K., Mottl, M.J., Nielsen, S.H.H., IODP Expedition 331 Scientists, 2012. IODP Expedition 331: Strong and Expansive Subseafloor Hydrothermal Activities in the Okinawa Trough, Scientific Drilling 13, 1927.

Thornton, B., Ura, T., 2011. Effects of pressure on the optical emissions observed from solids immersed in water using a single pulse laser. Appl. Phys. Express 4, 022702.

Thornton, B., Takahashi, T., Ura, T., Sakka, T., 2012a. Cavity formation and material ablation for single-pulse laser-ablated solids immersed in water at high pressure. Appl. Phys. Express 5, 102402.

Thornton, B., Masamura, T., Takahashi, T., Ura, T., Ohki, K., Sakka, T., 2012b. Development and field testing of laser-induced breakdown spectroscopy for in situ multi-element analysis at sea. In: Proceedings of MTS/IEEE Oceans '12, Hampton Roads, 120514-002.

Thornton, B., Sakka, T., Takahashi, T., Tamura, A., Masamura, T., Matsumoto, A., 2013. Spectroscopic measurements of solids immersed in water at high pressure using a long duration nano second laser pulse. Appl. Phys. Express 6, 082401.

Thornton, B., Sakka, T., Masamura, T., Tamura, A., Takahashi, T., Matsumoto, A., 2014a. Long-duration nano-second single pulse lasers for observation of spectra from bulk liquids at high hydrostatic pressures. Spectrochim. Acta Part B 97, 7–12.

Thornton, B., Sakka, T., Ohki, K., 2014b. Component Analysis Device. Patent No. PCT/JP2013/074729.

Tognoni, E., Cristoforetti, G., Legnaioli, S., Palleschi, V., Salvetti, A., Mueller, M., Panne, U., Gornushkin, I., 2007. A numerical study of expected accuracy and precision in calibration-free laser-induced breakdown spectroscopy in the assumption of ideal analytical plasma. Spectrochim. Acta Part B 62, 1287–1302.

Tognoni, E., Hidalgo, M., Canals, A., Cristoforetti, G., Legnaioli, S., Palleschi, V., 2009. Towards a calibration-less ICP-AES method for the determination of trace elements in aqueous solutions: double ratio plasma diagnostics combined with an internal standard. J. Anal. At. Spectrom. 24, 655–662.

Tognoni, E., Cristoforetti, G., Legnaioli, S., Palleschi, V., 2010. Calibration-free laser-induced breakdown spectroscopy: state of the art. Spectrochim. Acta Part B 65, 1–14.

Ueno, H., Hamasaki, H., Murakawa, Y., Kitazono, S., Takeda, T., 2003. Ore and gangue minerals of sulfide chimneys from the North Knoll, Iheya Ridge, Okinawa Trough, Japan. JAMSTEC J. Deep Sea Res. 22, 49–62.

UNESCO, 1981. Background Papers and Supporting Data on the International Equation of State of Seawater 1980. UNESCO Technical Paper in Marine Science 38, 192pp.

Wachter, J., Cremers, D., 1987. Determination of uranium in solution using laser-induced breakdown spectroscopy. Appl. Spectrosc. 41, 1042–1048.

Wainner, R.T., Harmon, R.S., Miziolek, A.W., McNesby, K.L., French, P.D., 2001. Analysis of environmental lead contamination: comparison of LIBS field and laboratory instruments. Spectrochim. Acta Part B 56, 777–793.

Whitehouse, A.I., Young, J., Botheroyd, I.M., Lawson, S., Evans, C.P., Wright, J., 2001. Remote material analysis of nuclear power station steam generator tubes by laser-induced breakdown spectroscopy. Spectrochim. Acta, Part B 56, 821–830.

Wiens, R.C., Arvidson, R.E., Cremers, D.A., Ferris, M.J., Blacic, J.D., Seelos IV, F.P., Deal, K.S., 2002. Combined remote mineralogical and elemental identification from rovers: field and laboratory tests using reflectance and laser-induced breakdown spectroscopy. J. Geophys. Res. Planets 107, 2156–2202.

Wiens, R.C., Maurice, S., Barraclough, B., Saccoccio, M., Barkley, W., 75 more of the ChemCam Team, 2012. The ChemCam instrument suite on the Mars Science Laboratory (MSL) rover: body unit and combined system tests. Space Sci. Rev. 170, 167–227.

Wiens, R.C., Maurice, S., Lasue, J., Forni, O., Anderson, R.B., Clegg, S., Bender, S., Blaney, D., Barraclough, B.L., Cousin, A., Deflores, L., Delapp, D., Dyar, M.D., Fabre, C., Gasnault, O., Lanza, N., Mazoyer, J., Melikechi, N., Meslin, P.Y., Newsom, H., Ollila, A., Perez, R., Tokar, R.L., Vaniman, D., 2013. Pre-flight calibration and initial data processing for the ChemCam laser-induced breakdown spectroscopy instrument on the Mars Science Laboratory rover. Spectrochim. Acta Part B 82, 1–27.

Yamamoto, K.Y., Cremers, D.A., Monty, J.F., Foster, L.E., 1996. Detection of metals in the environment using a portable laser-induced breakdown spectroscopy instrument. Appl. Spectrosc. 50, 222–233.

Zhang, X., Walz, P.M., Kirkwood, W.J., Hester, K.C., Ussler, W., Peltzer, E.T., Brewer, P. G., 2010. Development and deployment of a deep-sea Raman probe for measurement of pore water geochemistry. Deep-Sea Res. I 57, 297–306.